Master Thesis

Studying the effect of strain on the mechanical properties of wrinkled graphene

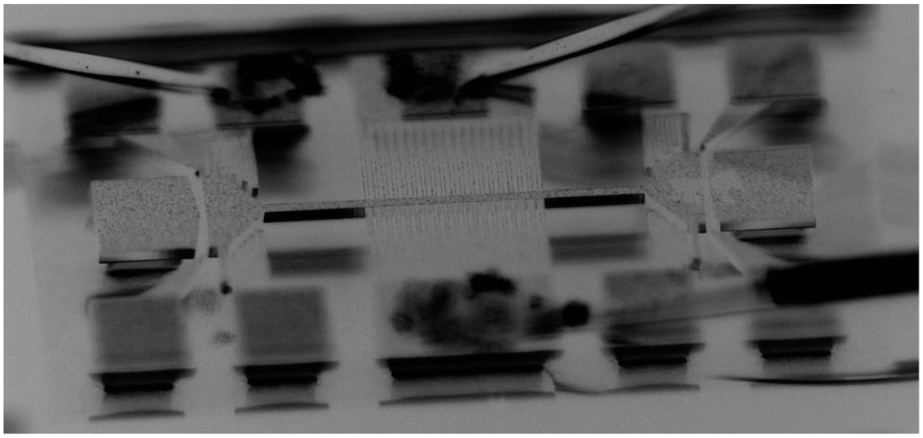

Author:
Izak de Heer

Supervisors:
Prof. dr. Peter Steeneken[1,2]
Dr. Gerard Verbiest[1]
MSc. Hanqing Liu[1]
[1]*Department of Precision and Microsystems Engineering*[2]
Department of Quantum Nanoscience, TU Delft

May 13, 2022

Abstract

Surface corrugations in graphene negatively effect the unique and useful properties of graphene. In order to exploit the special properties of graphene, it is therefore important to understand the phenomenon of wrinkling. In this study, strain engineering was applied to study the flattening of wrinkles in a suspended graphene membrane. Initially, a MEMS device was used for inducing strain in a suspended membrane. Transfer of graphene onto the MEMS device was challenging and in this study not successful. Suspended graphene drums with an electrostatic backgate were used as an alternative system for strain engineering. A stress-strain curve was calculated from the drum deflection measurements as a function of backgate voltage. The stress-strain curve exhibits a non-linear regime that is due to wrinkle flattening and a linear regime that is due to membrane stretching. The Young's modulus of the membrane is determined using three different methods. An analytical model for the stress-strain curve of a wrinkled membrane proposed in [1] is fitted to the experimental data. The good agreement between the model and the data validates the model and provides insight into the parameters that govern the behavior of the membrane. Wrinkles were visualized individually and were clearly decreasing in size with increasing backgate voltage. Also the surface correlation length was shown to increase with backgate voltage, indicating flattening of wrinkles.

Contents

Chapter 1

Introduction

1.1 History of graphene

Graphene is a 2-dimensional (2D) material consisting of a single layer of carbon atoms, arranged in a hexagonal lattice. Many layers of graphene stacked together constitute the naturally occurring material graphite. Strictly speaking, the term graphene belongs to a single layer of graphite. However, the term graphene has been used for few-layer and multilayer graphene as well. The structure of graphite with its stack of hexagonal layers was unravelled by powder diffraction experiments in 1917 [2]. With knowledge about the highly symmetric atomic structure of graphene, in 1947 Wallace investigated its unique electronic properties using the tight binding model [3]. In the following years, physicists realized that the linear dispersion relation that follows from the tight binding model for graphene implies exotic electron behavior. It was shown that electrons in graphene behave as massless Dirac fermions, which are relativistic particles [4].

Because of its highly symmetric and relatively simple atomic structure, graphene was used as a model system for theoretical studies about 2D materials. Along with theoretical studies, effort was put in producing monolayer graphene samples for experiments. Graphene was isolated for the first time by Geim and Novoselov in 2004 [5]. Geim and Novoselov introduced the Scotch tape method for mechanical exfoliation of graphite to produce micrometer-sized flakes of few-layer and even monolayer high-quality graphene. This cheap and easy but effective method triggered a gold rush among researchers to demonstrate the theoretically predicted properties of graphene. The zero bandgap [5], ultrahigh electron mobility [6], ultrahigh stiffness [7], high thermal conductivity [8], high transparency [9], chemical inertness [10], impermeability [11] and electromechanical tunability [12] of graphene were shown within a few years time. Graphene has also shown useful as a model system for experiments on quantum electrodynamics phenomena [13]. In 2018, it was discovered that bilayer graphene becomes superconducting when the angle between the layers equals the *magic* angle [14].

Although graphene is fascinating from a theoretical physics perspective, it also has the potential to revolutionize different fields of technology. Combining its unique properties with the fact that graphene is atomically thin results in a plethora of technological applications for microsensor devices, composite materials, surface coating, microelectronics, spintronics, valleytronics and superconductors.

1.2 Graphene surface corrugations

Theoretical predictions of the properties of graphene often rely on the highly symmetric, strictly 2D atomic arrangement of carbon atoms in graphene. In reality graphene is not perfectly flat, but tends to wrinkle and crumble. This is because a flat 2D system in free space is unstable at finite temperature, as described by the Mermin-Wagner theorem. This theorem states that long-range fluctuations in low-dimensional systems cost little energy and are favored since they increase the system's entropy [15]. Flexural phonons, which are thermal out-of-plane vibrations, stabilize an unsupported 2D membrane by balancing the entropy gain due to surface fluctuations with the energy loss due to bending and stretching. The flexural phonons form dynamic ripples in the membrane surface with a typical lateral size of tens of nanometers and a typical out-of-plane deflection of nanometers, as was shown for a graphene membrane in [16] using simulations and in [17] experimentally.

Besides the ripples that form due to flexural phonons, there are other types of corrugations in graphene. In the literature, surface corrugations are divided into three categories; wrinkles, crumples and the aforementioned ripples [18], as shown in figure 1.1. Wrinkles and crumples are not intrinsic to 2D membranes, as ripples are, but are due to external straining of the membrane.

In contrast to ripples, which are intrinsic to graphene, wrinkles and crumples only occur in graphene under external stress. The mechanism behind wrinkling is the minimization of bending and stretching energy given the strain field in the membrane. The bending and stretching energies are macroscopic descriptions of interatomic interactions between the carbon atoms in graphene. Wrinkles are characterized by a high aspect ratio of ~ 10 or higher and commonly appear as straight lines. These elongated deformations form in the direction of straining. Crumples result from compressive multiaxial stress. When the stress in crumpling graphene exceeds a certain threshold, the graphene sheet folds into a ball. Crumpling of graphene is the same physical process as crumpling a sheet of paper.

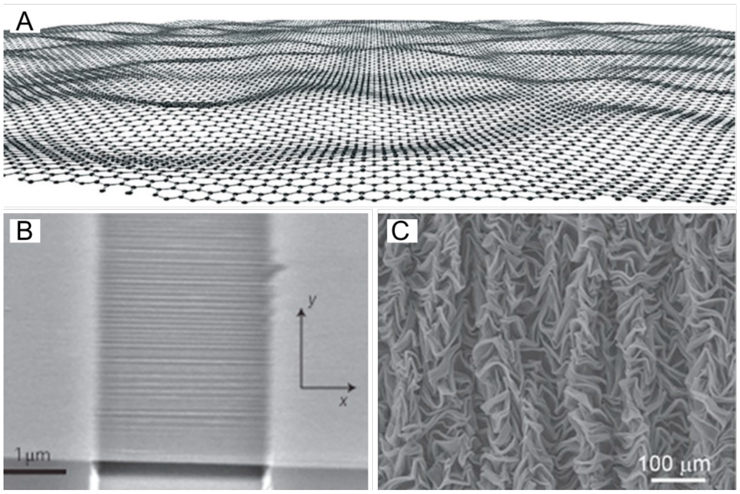

Figure 1.1: Different corrugation types in graphene; **A**) ripples, **B**) wrinkles and **C**) crumples. Figures are taken from [17], [19] and [20]

1.2.1 Impact of corrugations on material properties

Surface corrugations strongly affect the material properties of graphene. The special properties of graphene are partly because of its symmetric atomic structure. The symmetry because of equal carbon-carbon bond lengths is destroyed by non-uniform straining of the membrane. Curvature of the membrane affects the overlap of the p-orbitals, thus changing the π-orbitals. The π-orbitals, which are hybridized p-orbitals forming a spread-out electron cloud on both sides of the graphene lattice gives graphene its high electrical conductivity and chemical inertness. Corrugations reduce electrical conductivity due to increased charge carrier scattering [21], reduce thermal conductivity [22], induce electron-hole puddle formation [21], increase its chemical reactivity [23] and gas permeativity [24] and change the band structure [21]. Corrugations also induce charge inhomogeneity, create strong local pseudomagnetic fields [25] and make material properties anisotropic [26].

Understanding the physics of wrinkling is essential in order to pave the way for groundbreaking applications of graphene. On the other hand, the phenomenon of wrinkling itself may proof to have useful applications of its own, for instance increasing the out-of-plane stiffness of a membrane [27] or increasing its elastic deformation range. Since wrinkles are the result of a strain fields, a natural way to control wrinkles is to apply external stress to the membrane. Molecular dynamics simulations [1] and experiments [28] have shown that increasing strain leads to a decrease in the degree of wrinkling.

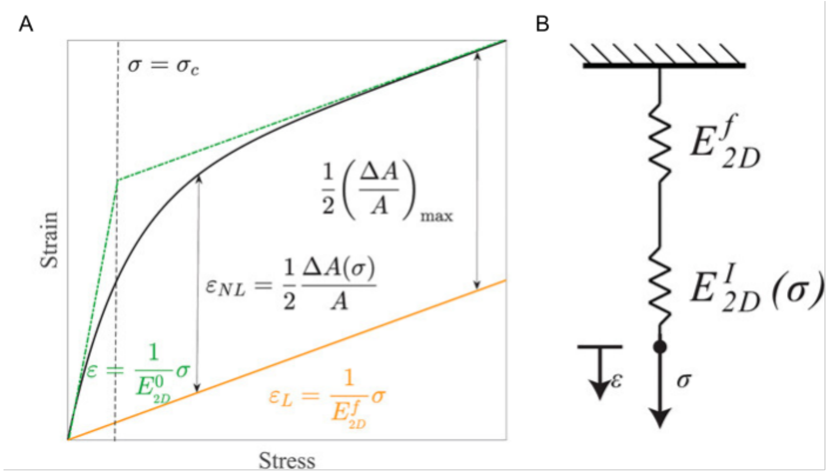

Figure 1.2: **A)** stress-strain curve for an unwrinkled membrane (orange) and a wrinkled membrane (black) with its bilinear approximation (green). **B)** model for the deflection of a wrinkled membrane, consisting of a linear spring (E^f_{2D}) modelling the intrinsic stiffness of the membrane and a non-linear spring ($E^I_{2D}(\sigma)$) modelling the flattening of wrinkles. Figure from (Sarafraz *et al.*, 2021)[1]

1.2.2 Simulations on graphene wrinkling

MD simulations on wrinkling of graphene done in the research group ahve shown that wrinkles in a suspended 2D membrane lead to a non-linear stress-strain curve [1]. An analytical bilinear model for the non-linear stress-strain curve is shown in figure 1.2. The model consists of the equations

$$\epsilon(\sigma) = \begin{cases} \frac{1}{E^0_{2D}}\sigma, & \sigma > \sigma_c, \\ \frac{1}{E^f_{2D}}\sigma + \frac{1}{2}\left(\frac{\Delta A}{A}\right)_{\max}, & \sigma < \sigma_c \end{cases} \tag{1.1}$$

where E^0_{2D} and E^f_{2D} are the tangential stiffness and Young's modulus. The degree of wrinkling is quantified using the notion of hidden area ΔA, which is the difference between the membrane surface area and the membrane 2D projection area. The value σ_c is the critical stress at which the transition from a wrinkled to a flat membrane occurs. $(\Delta A/A)_{\max}$ is the intercept of the linear stress-strain relation in the second regime with the strain axis. The two regimes correspond to a situation of flattening out wrinkles and a situation of straining of the carbon-carbon bonds. Flattening of wrinkles results in non-linear stiffness of the membrane. Molecular dynamics simulations were performed on a 20 by 20 nm square suspended monolayer graphene membrane at 4 K using the Tersoff potential. Strain was simulated by displacing the fixed boundaries outwards. The MD simulations confirmed the analytical model shown in figure 1.2.

1.3 Manipulating wrinkles in graphene

1.3.1 Strain engineering methods

Because surface corrugations have a negative effect on the special properties of graphene, much effort is put in understanding, controlling and removing graphene wrinkles. Understanding the phenomenon of wrinkling is highly relevant for industrial applications of graphene. This is because the main method for high-throughput large scale graphene production, which is chemical vapor deposition (CVD), unavoidably introduces wrinkles. Wrinkles arise in CVD graphene during the cooling step after growing graphene at high temperature, due to a thermal expansion coefficient (TEC) mismatch between graphene and the substrate on which it is grown.

One way to reduce wrinkling of CVD graphene is to use an extremely flat substrate with a TEC similar to graphene to grow graphene [29]. Minimizing the formation of wrinkles by tuning the CVD substrate is useful, but it answers only part of the question of how to obtain flat graphene. In many applications, CVD graphene has to be transfered from the substrate onto which is was grown to another substrate for experiments. The transfer process is often done by releasing the graphene from the substrate in liquid, after which it will float on the liquid and can be picked up using the target substrate. During the transfer process, liquid surface adhesion forces generate strain in the membrane, leading to wrinkles and folds [30]. The same will happen during mechanical exfoliation and subsequent transfer of graphene to the target substrate using a polymer stamp [31], which is the basis of the Scotch tape method. Also surface imperfections in the target substrate can lead to strain in the membrane that is transfered on top of it. It is not possible to grow graphene suspended over a gap, thus for making suspended graphene membranes, transfer will always be necessary. Therefore, it is most useful to flatten graphene only after transfer to the sample under investigation.

In the literature, different methods have been presented to tune the wrinkling of suspended graphene, such as thermal expansion of a trench with graphene suspended across [19], gel cracking [32], suspending graphene over nanopillars [33] and gas pressure deflection [28][34]. More methods have been used to induce strain in a suspended membrane, but not for the purpose of manipulating wrinkles, such as AFM indentation [7], substrate bending [35] and electrostatic backgating [36].

Microelectromechanical (MEMS) systems have also been used to control strain in 2D membranes. A MEMS device is a structure, usually made of silicon, ranging from microns to millimeters in size, with components of micrometer scale. In the nanotechnology industry, MEMS devices serve as small-scale accelerometers, gyroscopes, resonators, micromirror controllers, displacement sensors, etc. Due to their large surface to volume ratio, electrostatic forces

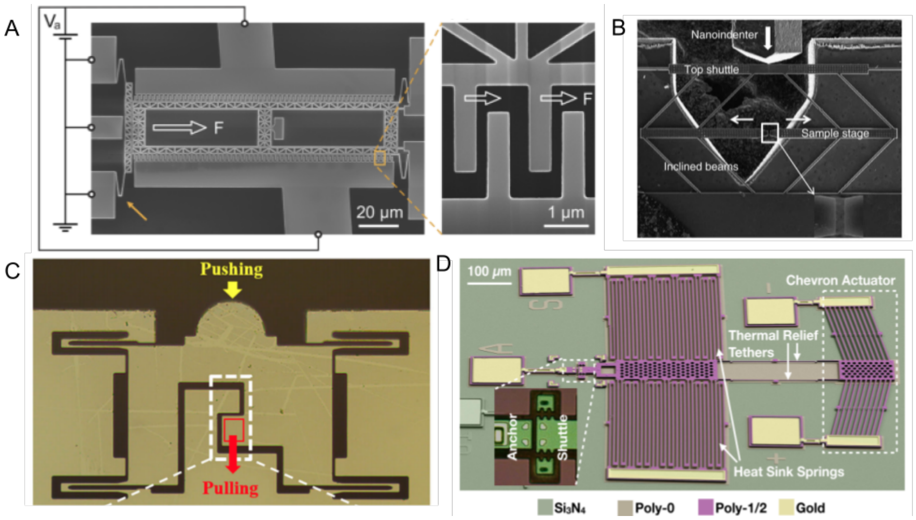

Figure 1.3: **A**) electrically actuated [37], **B**,**C**) push-to-pull [38][39] and **D**) thermally actuated [40] MEMS devices.

and viscous forces such as surface tension and surface adhesion dominate the behavior of a MEMS.

In a MEMS device designed for strain engineering, the main component is a movable structure suspended with springs that can pull on a membrane. There are three strain engineering MEMS designs presented in the literature, each one with a different method to move the suspended structure, see figure 1.3. The three types are referred to as push-to-pull MEMS [38][39], thermally actuated or Chevron actuator MEMS [40][41][42] and electrically actuated or comb-drive actuator MEMS [37][43][44][45][46]. Moving the suspended structure in a push-to-pull MEMS requires a nanomanipulator, that can accurately exert a small force on a specific surface designed for this purpose. Thermally actuated MEMS move by thermal expansion of spring beams. The most common way to move a suspended MEMS structure is to apply an electric potential over not-connected MEMS components, creating electrostatic forces that will move the structure.

MEMS devices have been used to study fracture strength [38] and Young's modulus [39] of graphene, as well as the resonance frequency tunability [43][44] and quantum hall effect tunability [45]. Other studies used MEMS devices to reach high strain values in molybdenum disulfide (MoS_2) [40] and graphene [41][42], to tune the resonance frequency of a suspended graphene membrane [43][44][47] and to map the strain field in graphene [37].

1.3.2 MEMS platform for strain engineering

In this study, a MEMS device serves as a platform to exert in-plane tensile force on a 2D membrane. The use of a MEMS device has several advantages over alternative methods, such as membrane indentation measurements, bulge test measurements, thermal expansion or substrate bending measurements. The main advantage of a MEMS device is that its functionality is completely determined by design, which makes it a versatile tool for a wide variety of applications. Parameters such as geometry, stiffness, force magnitude and direction, stress distribution, capacitance, resonance frequencies and resonance mode shapes are controlled by design. The behavior of a MEMS device is predictable and can be modelled analytically or numerically.

A MEMS device provides in-plane loading of a membrane, whereas other methods for strain engineering exert out-of-plane forces on the membrane. Although thin membranes are assumed to have negligible bending rigidity making both methods equivalent, it has been shown that wrinkling of graphene membranes increase the bending rigidity significantly [27]. By using only in-plane forces, the in-plane mechanical properties such as stiffness are decoupled from out-of-plane mechanical properties such as bending rigidity. Yet another important advantage of straining a membrane using a MEMS device is that the strain can be continuously, reversibly and dynamically controlled at high rate.

For this study, a dedicated MEMS device is designed for applying in-plane tension and compression using electrostatic comb-drive actuators. An image of the MEMS device is shown in figure 1.4. The images in figure 1.4 and all optical microscope images are made with a Keyence VHX-6000 digital microscope, if not mentioned otherwise. The MEMS device is part of a collection of different MEMS structures on a single chip designed by Dr. Satadal Dutta and manufactured by the commercial foundry X-FAB[1]. X-FAB specializes in fabricating microscale suspended, movable, 3D silicon structures, using etching methods that can make structures with a minimum size of 2 micron. Since fabricating a MEMS device without automated equipment is a laborious process, requires complex equipment and has low throughput, ordering devices from commercial manufacturers that use high-throughput processes is a promising possibility to make MEMS-based research more accessible.

1.4 Research goals

This study will focus on investigating the effect of strain on wrinkles in graphene by visualizing the wrinkles directly. Although experimental and simulation studies have been done, wrinkles have not been directly visualized as a function of strain experimentally. Direct visualization of the wrinkles as a function of strain could provide new insight in how wrinkles change upon straining the

---

[1] website: https://www.xfab.com/

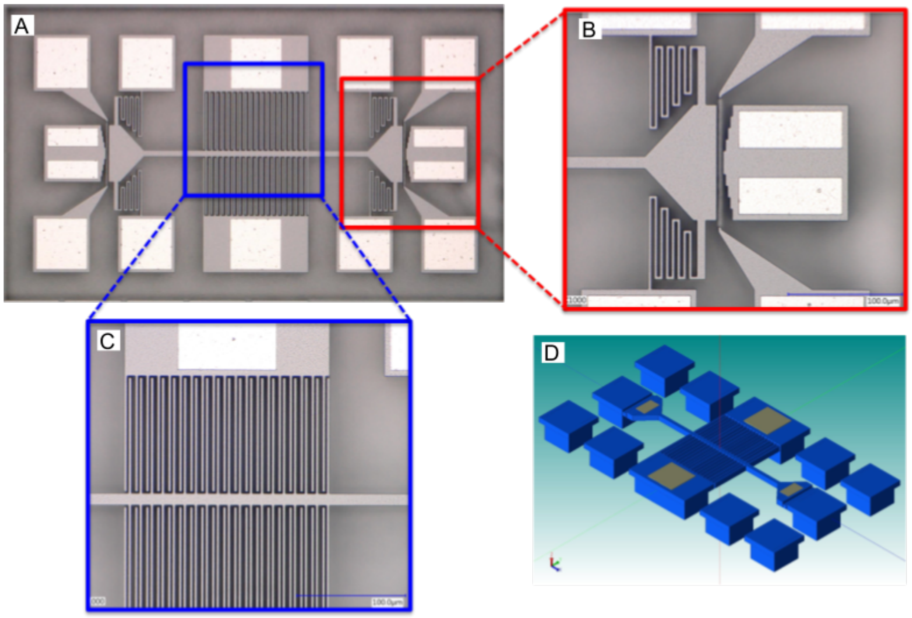

Figure 1.4: **A)** optical image of the MEMS device with close ups of **B)** the spring structures with the transfer area and **C)** the comb-drive fingers. **D)** shows a 3D design where the fixed electrodes and the suspended comb are visible.

membrane. The main goals of this study is to measure the stress-strain curve of a suspended wrinkled graphene membrane, where the transition from wrinkled to flat graphene appears as a change in Young's modulus as predicted in [1]. The analytical model will be evaluated using experimental data. The second goal is to visualize a membrane that undergoes the transition from wrinkled to flat, with sufficient resolution to distinguish individual wrinkles. The MEMS device will be used to induce strain in the membrane and the membrane will be visualized using optical interferometry.

In chapter 2, three optical interferometry methods that are used in this study are described and compared. The MEMS device characterization by simulations and experiments will presented in chapter 3. In order to obtain a stress-strain curve, the relation between bias voltage and applied force by the device needs to be determined to convert voltage into stress. For this purpose an empty MEMS device will be characterized, but also vertical displacement, vertical stiffness and resonance frequencies will be measured. Following these preparation steps, experiments will be done on the MEMS device with a membrane on top. Transfer of the membrane and MEMS measurements are the topic of chapter 4. Since the transfer process will be a major challenge, an alternative method for straining a membrane will be used as well. This alternative method uses an electrostatic backgate to deflect a graphene drum. Theory and measurements on graphene drums are described in chapter 5. Chapter 6 presents the conclusions from this study.

Chapter 2

Optical interferometry measurement methods

2.1 Visualizing wrinkles in a 2D membrane

The purpose of this study is to investigate the behavior of graphene wrinkles under strain. In the literature, flattening of wrinkles has been measured indirectly by comparing intrinsic strain based on Raman shift and geometric strain based on membrane deflection [28]. In this study, the membrane surface will be imaged as a function of strain directly with sufficient resolution to distinguish individual wrinkles. The measurement method has to meet three conditions in order to be suitable for the experiments in this study.

- The methods should be able to measure the displacement of the MEMS structure and visualize the topology of the membrane spanning the structure simultaneously.
- Since surface corrugations such as wrinkles and crumples are affected by minute forces [48], a non-invasive measurement method is preferred.
- The measurement resolution in lateral and vertical direction should be sufficient to distinguish individual wrinkles. The corrugations are expected to have vertical dimensions of nanometers to hundreds of nanometers and lateral dimensions of tens of nanometers to micrometers.

Membrane topology, including wrinkles, is often measured using atomic force microscopy (AFM), because AFM has an subnanometer resolution in the lateral and vertical directions. The major drawback of AFM for wrinkle imaging is the tip-membrane interaction during the measurement, that could change the surface topology. Besides, the tip-membrane interaction is likely to change the local electrical properties of the membrane. Although this last notion will not be relevant in this study, it can become important in the future when the conductance of the membrane is measured simultaneously. Since the displacement of the MEMS structure needs to be determined for each bias voltage, it is necessary to image the edges of the structure. AFM also has difficulty measuring steep vertical jumps, so it may not be able to measure the device displacement accurately. Although it is of less importance, AFM measurements are relatively time-consuming compared to optical imaging.

Another non-contact imaging method with in principle high resolution is electron microscopy. The problem of electron microscopy in this case it the fact that electron irradiation may induce defects in the atomic structure of the membrane and potentially break the membrane. Charging effects due to electron irradiation can also affect the bias voltage over the comb-drive actuators, thereby introducing inaccuracy in the force control. There is also no electron microscope available for this study that is stable enough to provide the required resolution.

Optical measurement methods provide a better solution in this situation, since they are non-invasive and do not alter the electrical properties of the membrane. However, optical methods have relatively low resolution due to the optical diffraction limit, which is around 200nm. Diffraction limited resolution does not meet the required vertical resolution, which needs to be nanometer-scale in order to visualize wrinkles. However, the vertical resolution can be reduced to subnanometer scale by using interferometric optical imaging. The basic principle of interferometric imaging is interference between a coherent object beam and a reference beam, where information about the object surface topology is encoded in the phase of the interfering beams. There exist multiple interferometric profilometry methods that all have advantages and disadvantages. The three different methods that will be used in this study will be briefly introduced for proper understanding of the measurement results.

2.2 Monochromatic interferometry

In this study, a Lynceetec Digital Holography Machine (DHM) R2200 microscope system[1] is used to do monochromatic interferometry measurements. Monochromatic interferometry uses light of a single frequency to create an interference pattern between light reflected from the sample and a reference beam. The Lynceetec uses a 675 nm laser for monochromatic measurements. The optical paths of the microscope are shown in figure 2.1A. The object (O) beam reflects from the sample and interferes with the reference beam. The phase difference due to an optical path length difference between the beams generates the interference pattern, described by the equation

$$I(x,y) = 2I_0\cos(\phi(x,y) + \phi_0), \tag{2.1}$$

where I_0 is the intensity of the object and reference beam, here assumed to be equal, $\phi(x,y)$ is the phase of the object beam depending on the height of

---

[1] website: https://www.lynceetec.com/reflection-dhm/

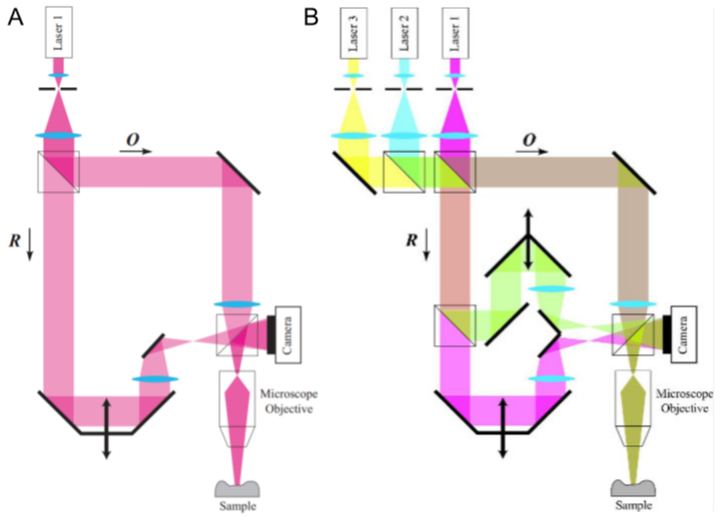

Figure 2.1: Schematic of the optical system of the Lynceetec HDM in **A)** monochromatic mode and **B)** multi-wavelength mode(source: Lynceetec user guide)

the sample at position x, y and ϕ_0 is a known phase shift between object and reference beam. The movable mirror can be manually adjusted to optimize the coherence between the object and reference beam. A tunable polarization filter adjusts the intensity of reference beam so that it is equal to the intensity of the reflected object beam. Since the topology of the sample is encoded into light intensity by interference, the vertical resolution of the microscope can reach subnamometer values. The important limitation of this method is that steep steps in the sample surface higher than half the wavelength cannot be measured with certainty, since phase difference is periodic. A step of more than half the wavelength can be any multiple of 2π lower or higher than measured. This means that the vertical range of monochromatic interferometry is small. If the sample is sufficiently smooth, it is possible to reconstruct phase jumps on a surface using a technique called phase unwrapping. However, it is hard for a phase unwrapping algorithm to discern phase steps from steep vertical steps in the sample. Phase unwrapping is also hard on a highly wrinkled graphene membrane. In general, monochromatic interferometry is used for subnanometer resolution measurements on smooth and continuous surfaces. The Lynceetec has a 100x and 40x objective with lateral resolutions of 0.38 μm and 0.45μm respectively.

	Laser 1	Laser 1+2	Laser 1+3
Wavelengths	675 nm	675 nm + 794 nm	666 nm + 675 nm
Beating wavelength	-	4.4 μm	50 μm
Vertical resolution	0.30 nm	6.0 nm	40 nm
Max. height of steep steps	333 nm	2.1 μm	24 μm

Table 2.1: Lynceetec specifications for monochromatic and multiwavelength measurements. Source: Lynceetec

2.3 Multiwavelength interferometry

An adaptation to monochromatic interferometry that increases the vertical range is to use light of multiple wavelengths, rather than a single wavelength. Interference between the multiple frequencies in the object and reference beam create a beating pattern with a low and high frequency component, according to the trigonometric identity

$$\sin(\theta_1) + \sin(\theta_2) = 2\sin(\frac{\theta_1 + \theta_2}{2})\cos(\frac{\theta_1 - \theta_2}{2}). \tag{2.2}$$

The low frequency component of this mixing signal has a higher wavelength λ_{12} compared to the original wavelengths λ_1 and λ_2, see figure 2.2A,B. The Lynceetec DHM R2200 contains 3 different lasers with 666 nm, 675 nm and 794 nm wavelength, that allow for multiwavelength interferometry. The vertical step height that can be measured increases from 333 nm for monochromatic interferometry to 2.1 μm and 24 μm for multiwavelength interferometry. The disadvantage of using a beating frequency for higher vertical range is the lower vertical and lateral resolution. To take advantage of both the resolution of monochromatic and the vertical range of multiwavelength interferometry, the Lynceetec software has the functionality to map both these measurements together. The specifications of different measurement modes of the Lynceetec are shown in figure 2.1.

2.4 White light interferometry

A white light interferometer uses light with a continuous frequency spectrum. The intensity of a coherent multichromatic light beam due to interference has a peak at the position where the phase difference between all frequency components is zero and quickly decays away from this point, see figure 2.2C. In white light interferometry, this peak is used to determine the height profile of a sample. The interference pattern will be visible on a surface of the sample if the distance between this surface and the camera reaches some value. By moving the stage in the vertical direction, the interference pattern will be visible on different parts of the sample, indicating the height of the sample at that particular position. Since the interference pattern has only a few high peaks that decay

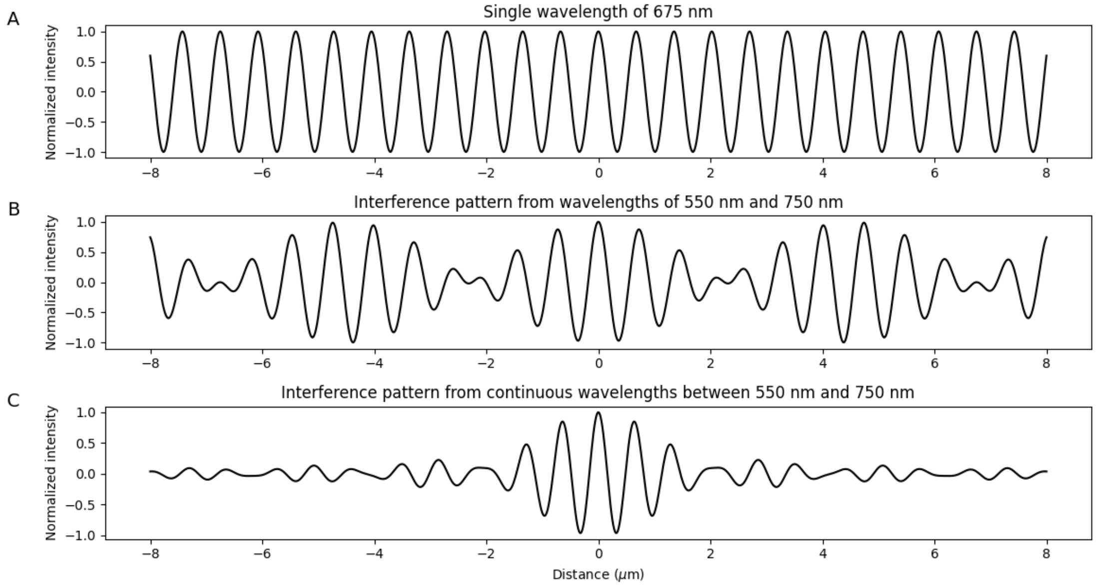

Figure 2.2: **A)** Spatial light intensity function of a monochromatic beam, **B)** multiwavelength beam and **C)** white light beam.

quickly and is thus not periodic, the height of the sample can always be uniquely determined. This implies that the vertical range of a white light interferometer is in principle equal to the vertical displacement range of the stage.

The disadvantage of white light interferometry is that its vertical resolution is lower compared to monochromatic or multichromatic interferometry. The reason for this lower vertical resolution is that the height of each pixel in the measurement is determined from the stage position at which the pixel intensity is maximal, which is limited by the accuracy of the stage displacement, rather than intensity differences due to interference. The main advantage of white light interferometry is that is gives an absolute value for the height of the sample at each pixel, even if the sample surface is rough or has steep edges. Therefore, it is often used to obtain a height profile of rough and discontinuous surfaces.

One factor that strongly affects the measurement accuracy of each interferometry method described, is the tilt of the sample. If the sample is tilted, the intensity of reflected light will be lower, resulting in a lower signal-to-noise ratio. Tilt also increases the height differences in the sample, which in the case of monochromatic or multiwavelength interferometry can give rise to phase jumps.

Chapter 3

MEMS device characterization

3.1 Description of MEMS structure

One of the advantages of a MEMS device is that its behavior is predictable and controllable. In order to understand the behavior of the MEMS device that is used in this study, a detailed description of the structure, as well as calculations and simulations is important. The structure, as shown in figure 1.4, has dimensions of roughly 880 μm by 520 μm. A cross section of the device is shown in figure 3.1, note that different components are not shown at the correct relative scale. The device consists of two wafers that are bonded together with an insulating oxide layer in between; the bottom wafer and the membrane wafer. In the bottom wafer is a cavity of 50 μm deep. Above this cavity is the suspended structure, which is etched into the membrane wafer.

Parts of the membrane wafer are isolated by oxide layers so that they can serve as electrodes. On top of the electrodes, there is 1 μm of aluminum serving as bond pad for wire bonding. The square bond pads are 80 μm by 80 μm in size. The membrane wafer is 15 μm thick, but can locally be reduced in height by an additional etching step. In the MEMS device, part of the membrane wafer is reduced in height by 5 μm to act as a back gate. A detailed description of the manufacturing process is given in [49].

Figure 1.4B shows one of the two transfer areas, with the back gate visible between the movable structure and the fixed structure. The gap over which a 2D membrane will be suspended is 6 μm in the narrowest part. The interdigitated comb fingers shown in figure 1.4C are 2 μm wide, 100 μm long and 15 μm deep. The fingers are spaced asymmetrically, being apart 2 μm on one side and 4 μm on the other, in order to fix the polarity of the device. One side of the structure allows for membrane compression and the other for membrane straining. The electrodes on the fixed side of the transfer area are meant for measuring electrical conductance of a membrane spanning the gap.

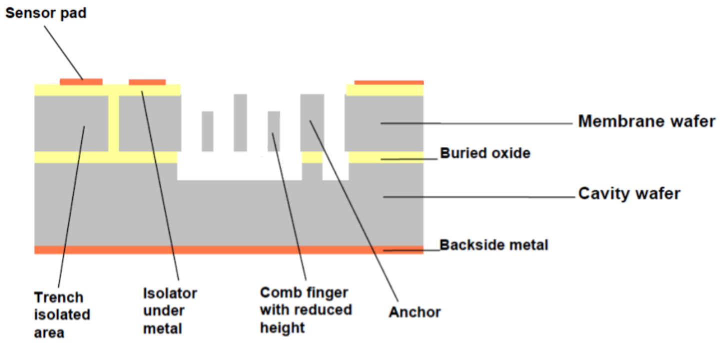

Figure 3.1: Cross section of general MEMS structure (not the design used in this study) showcasing all components of the device. Materials are colored as follows: grey for Si, yellow for SiO_2, orange for Al.

3.2 Stiffness of movable structure

One important parameter of the device is the stiffness of the springs that suspend the movable structure. Because of the complex shape of the spring, an approximation will be used to estimate its stiffness. Figure 3.2 shows how the spring can be approximated by simple springs in series. The spring constant of these simple springs is expressed as

$$k = \frac{3B}{l_1^3 + 3l_1^2 l_2 + 3l_1^2 l_3 - 3l_1 l_3^2 + l_3^3},$$

where l_1 and l_3 are the long sides, l_2 the short side of the structure and B is given by

$$B = \frac{bh^3E}{12},$$

where b, h and E are the structure width, thickness and Young's modulus respectively. Using $b = 2$ μm, $h = 15$ μm and $E = 160$ GPa for silicon, the beam lengths and spring constants of the simple springs are given in table 3.1. The spring constant of the full spring is approximately equal to that of simple springs 1 to 4 put in series, which is

$$k_{\text{spring}} \approx (\frac{1}{k_1} + \frac{1}{k_2} + \frac{1}{k_3} + \frac{1}{k_4})^{-1} = 125 \; Nm^{-1}.$$

The movable structure is supported by four identical spring structures. The four springs are arranged such that two parallel springs are in series with two parallel springs. The stiffness of the movable structure therefore is

$$k_{\text{structure}} = \left((k_{\text{spring}} + k_{\text{spring}})^{-1} + (k_{\text{spring}} + k_{\text{spring}})^{-1}\right)^{-1} = k_{\text{spring}} = 125 Nm^{-1}$$

	L_1 (μm)	L_2 (μm)	L_3(μm)	k (Nm^{-1})
Spring 1	80	3	72	241
Spring 2	62	3	62	505
Spring 3	52	3	52	839
Spring 4	42	3	42	1546

Table 3.1: Length of the simple spring beams with L_1 and L_3 the long and L_2 the short sides and the spring constant of the simple springs.

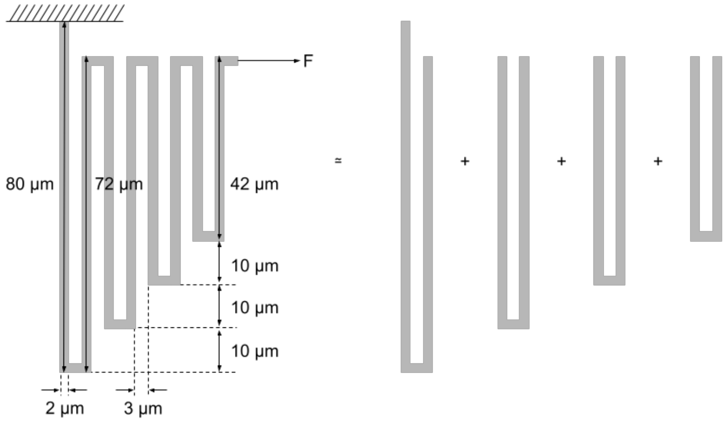

Figure 3.2: The stiffness of the springs that support the MEMS structure can be approximated as simple springs put in series.

3.3 Analytical model for electrostatic forces

The electrostatic forces between the interdigitated fingers are expressed analytically by approximating the fingers as parallel plate capacitors. This approximation is valid in the limit of large finger area compared to the inter-finger distance. Since the fingers are 15 μm by 100 μm in size and the inter-finger distance is 2 μm and 4 μm, this approximation is allowed.

Consider a comb finger with its two neighboring fingers. Since the distance between the fingers is asymmetric (see figure 3.3), there are different electrostatic force in opposite directions on the middle comb finger. Denote the displacement of the movable structure by x. The combined force due to both neighboring fingers can be found using the expression for energy stored in the capacitors, according to the following derivation

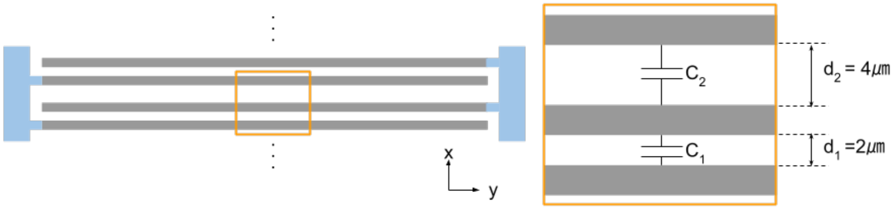

Figure 3.3: Schematic of the capacitances between the interdigitated fingers.

$$U = \frac{1}{2}CV^2 = \frac{n\epsilon A}{2d}V^2$$
$$F_e = -\frac{\partial U}{\partial d} = -\frac{\partial}{\partial d}\frac{n\epsilon_0 A}{2d}V^2 = \frac{n\epsilon_0 A}{2d^2}V^2 = \frac{CV^2}{2d}$$
$$F_{e,1} = -\frac{\partial U_1}{\partial d} = -\frac{\partial}{\partial(d_1-x)}\frac{1}{2}\frac{n\epsilon_0 A}{d_1-x}V^2 = \frac{n\epsilon_0 A}{2(d_1-x)^2}V^2$$
$$F_{e,2} = -\frac{\partial U_2}{\partial d} = -\frac{\partial}{\partial(d_2+x)}\frac{1}{2}\frac{n\epsilon_0 A}{d_2+x}V^2 = \frac{n\epsilon_0 A}{2(d_2+x)^2}V^2$$
$$F_e = F_{e,1} - F_{e,2} = \frac{n\epsilon_0 A}{2(d_1-x)^2}V^2 - \frac{n\epsilon_0 A}{2(d_2+x)^2}V^2 = \frac{n\epsilon_0 A[d_2^2 - d_1^2 + 2x(d_2+d_1)]}{2(d_2+x)^2(d_1-x)^2}V^2,$$

where d is the distance between the plates, $d_1 = 2$ μm and $d_2 = 4$ μm are the equilibrium distances between the fingers as shown in figure 3.3, n is the number of finger pairs in the structure, $A = 1.5 \cdot 10^{-9}$ m^2 is the overlapping area between two fingers and $\epsilon_0 = 8.85 \cdot 10^{-12}$ Fm^{-1} is the vacuum permittivity.

In order to find the relation between between voltage and displacement, the electrostatic force needs to be balanced with the spring force, resulting in the expression

$$k_{\text{structure}}x = \frac{n\epsilon_0 A[d_2^2 - d_1^2 + 2x(d_2+d_1)]}{2(d_2+x)^2(d_1-x)^2}V^2.$$

Since it is hard to express x in terms of V, this expression will not be inverted to find $x(V)$. For convenience, V will be expressed in terms of x as

$$V(x) = \sqrt{\frac{k_{\text{structure}}x}{\frac{n\epsilon_0 A[d_2^2-d_1^2+2x(d_2+d_1)]}{2(d_2+x)^2(d_1-x)^2}}}.$$

The inverted graph of x as function of $V(x)$ is shown in figure 3.4.

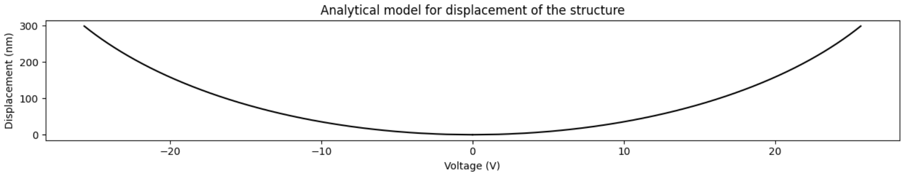

Figure 3.4: Inverted graph of $V(x)$, describing the voltage V that causes a displacement x of the movable structure.

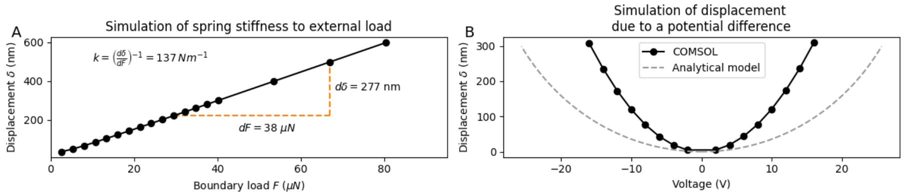

Figure 3.5: **A)** simulation of the stiffness of the movable structure using an external load and **B)** simulation of the displacement of the device due to a voltage applied over the comb-drive fingers.

3.4 COMSOL simulations of MEMS

For verification of the analytical calculations and for more elaborate analysis of its behavior, the MEMS device is simulated in COMSOL Multiphysics 6.0. The stiffness of the device was computed by applying a load on the suspended structure in x-direction. As shown in figure 3.5A, the structure stays in the linear stiffness regime for displacements that would induce up to 10% of strain in a suspended membrane. Since a strain of 10% in a membrane is very high, it can be assumed that the MEMS in-plane stiffness is linear in the displacement operating range. The stiffness equals the slope of the force-displacement graph, which is 137 Nm^{-1}. This value is close to the analytically estimated value of 125 Nm^{-1}, which is the first validation of the COMSOL model.

Figure 3.5B shows the simulation result for displacement and the analytical model as a function of comb-drive bias voltage. The analytical model does not agree with the COMSOL simulation. There are several possible explanations, for instance deviations in the device geometry from design values and the neglecting of fringing of the electric field between the fingers in the analytical model. Experimental characterization data will prove which curve agrees best with the actual behavior of the structure.

Although this study does not involve dynamic measurements, it is worth noting that dynamic measurements using a suspended structure can lead to mode coupling between resonances of the 2D membrane and the structure itself,

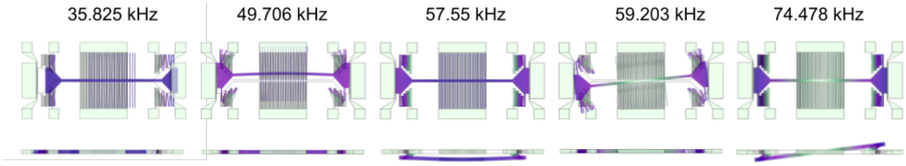

Figure 3.6: First five resonance modes of the suspended structure, simulated using COMSOL.

see for instance [47]. In order to recognize coupling between membrane and structure, it is useful to simulate the resonances of the structure and determine the resonance frequencies. The first five resonance modes are shown in figure 3.6. The first two and fourth resonance modes are in-plane modes and the third and fifth resonance modes are out-of-plane modes.

3.5 Experimental characterization of MEMS voltage-displacement curve

Although calculations and simulations provide valuable information about the MEMS device, it is essential to perform experimental characterizations of the device as well. The first characterization of the device is performed by measuring the displacement of the movable structure upon application of a voltage over the fingers. In order to make electrical contact with the MEMS device, the silicon chip containing the device is put in a chip carrier. In turn, the chip carrier is glued to a PCB using silver paint, such that the contacts of the chip carrier are connected to the contact electrodes of the PCB. Copper wires are soldered to the PCB electrodes to create a connection with a voltage source via the PCB. The last step is to connect the electrodes of the MEMS device to the contacts of the chip carrier. There are two wire bonding machines available for this study; a wedge bonder with aluminum wire and a ball bonder with gold wire. Figure 3.7 shows the bonds made by both machines. Since the needle of both wire bonding machines is larger than the bond pad, bonding is a difficult task. After testing both bonding methods, the wedge bonder appears to be more convenient since it can create bonds with smaller contact area. The wedge bonder used for the measured samples is a K&S model 4526 with aluminum wire.

For characterization of the MEMS device, the same method is used that will be used for studying the 2D material. This means that the displacement of the device has to be determined using interferometric optics. The measurements were performed with a Lynceetec Ditigal Holography Machine (DHM) model R-2200 using the 100x objective and the synthetic wavelength from combining lasers 1 (666 nm) and 3 (675 nm). Combining lasers 1 and 3 produces a long beating wavelength of 50 μm, using which vertical steps up to 24 μm can be measured and the out-of-plane accuracy is 20 nm. For this measurement, the

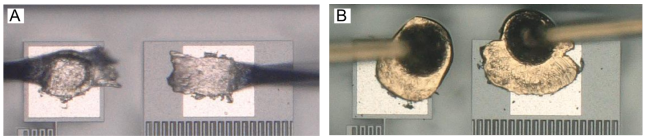

Figure 3.7: Wire bond connections made with **A** the wedge bonder and **B)** the ball bonder

Lynceetec was chosen above the white light interferometer, since its higher lateral resolution is important for determining small displacements of the movable structure.

The bottom of the trench in figure 3.8 displays a periodic pattern of lines in the Lynceetec height map, parallel to the edges of the trench. The facts that these lines have a regular shape and are parallel to the trench edges suggest this is a diffraction pattern. Since the height map is based on the phase of the reflected light, diffraction patterns can show up in the height map as artificial height differences. In order to prove the hypothesis that diffraction is creating these lines, the theoretical diffraction pattern is calculated. In the calculation, the top surface of the trench acts as the diffraction aperture. Since the distance between light source and the aperture is roughly 1 mm and the wavelength and aperture size are 50 μm and 6 μm respectively, the light source cannot be considered infinitely far way. This implies that the pattern has to be treated as Fresnel diffraction. The Fresnel integral for field propagation and diffraction is given as

$$E(x,y,z) = \frac{e^{ikz}}{i\lambda z} \int\int_{-\infty}^{\infty} E(x',y',0) e^{\frac{ik}{2z}\left[(x-x')^2+(y-y')^2\right]} dx'dy',$$

where $E(x',y',0)$ is the field in the initial plane, z is the propagation distance, λ and k are the wavelength and wave number of the light. For a rectangular aperture, it is convenient to split the integral over x' and y' into two separate integrals. This results into a sum of Fresnel sine and cosine integrals, given by

$$I(x,z) = \frac{1}{2}\left[|C(\alpha_2) - C(\alpha_1)|^2 + |S(\alpha_2) - S(\alpha_1)|^2\right],$$

where

$$\alpha_{1,2} = \sqrt{\frac{2}{\lambda z}}(x \pm a)$$

with a being half the width of the aperture. The Fresnel sine and cosine integrals $S(x)$ and $C(x)$ are given by

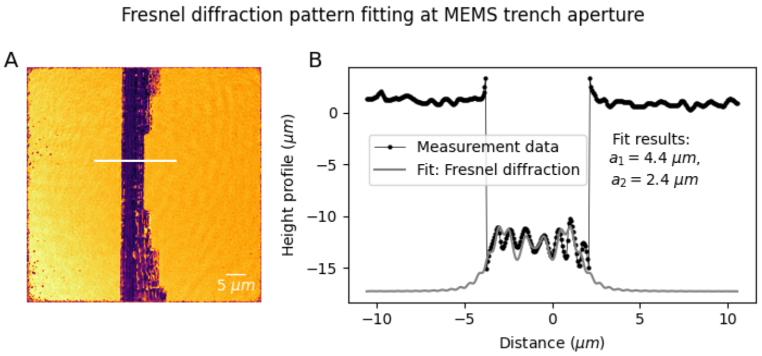

Figure 3.8: **A)** height map of the trench with the profile along the white line in **B)**. The pattern at the bottom of the trench can be fitted with a Fresnel diffraction pattern of the correct wavelength (675 nm, laser 3). The fitting parameters a_1 and a_2 correspond to the position of the two edges of the trench.

$$S(x) = \int_0^x \sin(t^2)dt$$
$$C(x) = \int_0^x \cos(t^2)dt.$$

Fitting the equation for Fresnel diffraction to the pattern found on the bottom of the MEMS trench results in good agreement between the fit and the data for the wavelength of laser 3, λ=675 nm. The fit is shown in figure 3.8. The values a_1 and a_2, corresponding to the positions of the edges of the trench, imply that the diffraction pattern matches an aperture of 6.6 μm wide, which is close to the actual width of 6 μm.

The bottom of the trench in the Lynceetec height map in figure 3.8A displays high noise, especially close to the stairs-shaped edge of the fixed part. Despite much effort, it is impossible to decrease the noise levels in the height map in this area. This noise is due to the high roughness of the surface of the bottom cavity beneath the trench. High roughness causes scattering of light, leading to noise in the interference signal that provides the height map. Multiple reflections in the cavity below the suspended structure may enhance this effect. Figure 3.9 supports this hypothesis by showing that the image quality is much better for a chip without bottom cavity, meaning that the MEMS structure is not suspended and the bottom is smooth. The comparison of suspended and not-suspended devices was possible since some chips in the batch produced by X-FAB did not have the bottom wafer cavity due to a manufacturing error.

In order to measure the displacement of the movable structure, the distance between the movable and fixed structures needs to be determined from the

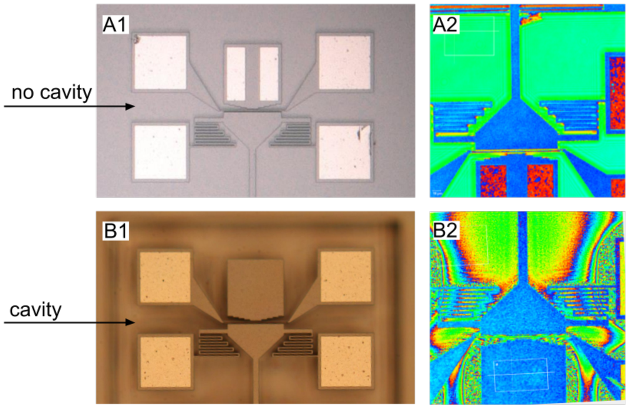

Figure 3.9: Comparison of **1)** optical and **2)** Lynceetec (20x objective) measurements of MEMS device **A)** without and **B)** with bottom wafer cavity.

height map. The necessary image analysis steps are shown in figure 3.10 and are described in detail below:

A Subtract a plane from the raw data if there is a tilt in the flat surfaces. Apply phase unwrapping if necessary.

B Crop the data so that only the parallel area of the trench, thus excluding the stairs-shaped region, remains.

C Apply a Gaussian filter to remove some noise from the data.

D Convert the image to binary values using a threshold filter. For this analysis, the mean threshold was applied since it provided the best result. Depending on the data quality, other thresholds may be more suitable.

E Perform an area opening operation in order to remove the black spots inside the white area. The area opening operation takes as input a threshold size. All black objects smaller than this threshold are removed.

F Perform an area closing operation in order to remove the white spots from the black areas, if there are any. In the example shown in figure 3.10F there is one tiny white area removed. Area closing is equivalent to area opening.

G Use a Sobel edge detection filter to detect the edges of the trench in the image.

H Fit a line through the pixels on the detected edge. Separating the pixels belonging to the two different lines can be done using geometrical conditions, or more generally using a clustering algorithm.

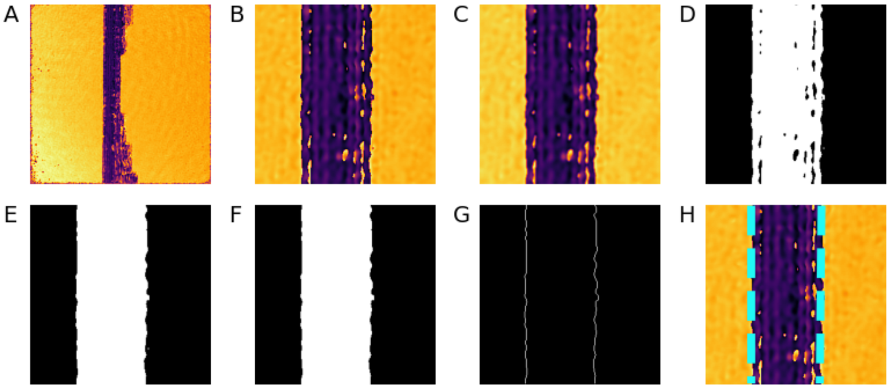

Figure 3.10: Image analysis steps for extracting the trench width from a height map; **A)** original image, **B)** crop of region of interest, **C)** Gaussian filter for noise reduction, **D)** binary image after applying mean threshold, **E)** area opening operation removes small black regions, **F)** area closing operation removes small white regions, **G)** edge detection on binary image, **H)** fit a line through the detected edge pixels to find the edge position

Once a linear function fit for both edges is determined, determining the distance between both edges is straightforward. In order to determine the displacement as a function of voltage, measurements were done with a varying DC voltage across the fingers. The voltage is swept from 0V to 12V, from 12V back to -12V and from -12V to 0V with measurements at intervals of 1V. This sweep across positive and negative voltages is important to detect possible hysteresis and charge offset in the structure. Each measurement is analyzed using the described image analysis procedure.

The experimental voltage-displacement results are shown in 3.11A. The displacement shows a quadratic dependence on voltage, with a coefficient a of 1.4 nmV^{-2}. The parabola is shifted towards the negative voltages by 0.63 V, which is the result of trapped charges on the suspended structure creating a small offset voltage. The measurement does not show hysteretic behavior, meaning the device moves as expected. The experimental data corresponds to the COMSOL simulation data, see figure 3.11B, since the value of coefficient a for the COMSOL model of 1.2 nmV^{-2} is close to the value of 1.4 nmV^{-2} found experimentally. The analytical model on the other hand appears to be inaccurate. The inaccuracy in the analytical model can be the result of an invalid approximation of the fingers as parallel plate capacitors, because of large fringe fields. This would explain why the results of the COMSOL simulation, where the capacitance is calculated numerically, are more accurate. However, it is doubtful that the fringe fields explain the large difference between the analytical model

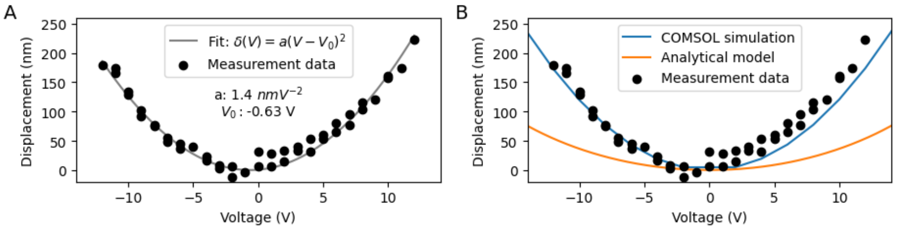

Figure 3.11: **A)** experimental data with a parabolic fit, with as fit parameters the proportionality constant a and offset voltage V_0. **B)** comparison of experimental data, COMSOL simulation and the analytical model for the displacement as function of the applied voltage.

and measurement. No proof is found for the discrepancy between the analytical model and the measured device behavior.

Since it is important that the device moves only in the lateral direction when varying the voltage over the comb fingers, the vertical displacement of the edges of the trench in the characterization measurement is analyzed. Figure 3.12A shows that both edges move downwards when the voltage increases. Since the downward movement of both edges is the same, the relative height difference is constant within the measurement uncertainty over the voltage sweep as shown in figure 3.12B. The observation that the relative difference between the edge heights does not change with comb-drive bias voltage suggests that the vertical movement is not related to the bias voltage. However, the correlation between absolute vertical position and voltage proves otherwise. The cause of the vertical movement is unclear, however it will not affect measurements since the relative difference between the edges is constant.

3.6 Experimental characterization of MEMS resonance modes

The Lynceetec microscope contains a stroboscopic module that can used to measure a frequency response spectrum. In order to measure the vertical resonances of the MEMS device, the device was put on a piezoelectric shaker. The stroboscopic module drives the piezoelectric element at high frequencies and measures at regular intervals. Since the image acquisition rate is relatively slow, measurements are done at a lower frequency compared to the signal frequency. The stroboscopic unit synchronizes the measurements and the driving signal such that measurements are done at regular intervals over multiple periods. The combined measurements form the response of the system to a single period of the driving signal.

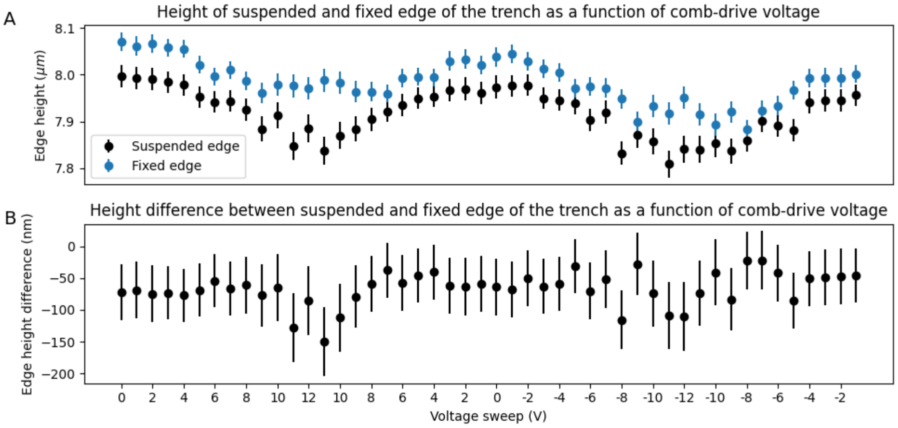

Figure 3.12: **A)** vertical position of the suspended and fixed edges of the trench and **B)** the height difference between the suspended and fixed edge, measured during the voltage sweep over the comb fingers.

For measuring the frequency response spectrum, the driving signal needs to be swept over a range of frequencies. Measurements are done on four MEMS devices, from two different chips using a signal with frequency bandwidth of 0.5 kHz. The response spectrum is averaged over three oscillation periods. The devices are not electrically connected while the resonances are measured. The frequency response spectrum is analyzed using the MEMS Analysis[1] tool of Lynceetec. The MEMS Analysis tool determines the amplitude of oscillation of a used-defined area in the sequence of measurements.

The resulting frequency response spectrum is shown in figure 3.13, displaying two resonance peaks at 80.5 kHz and 101.0 kHz. In order to confirm that the two resonance frequencies correspond to the first two vertical modes simulated using COMSOL, the vertical position of different areas of the structure is plotted, see figure 3.14. The mode at 80.5 kHz is a movement of the structure in the vertical direction, without angular movement. The mode at 101.0 kHz also is a movement of the structure in the vertical direction, but with both sides of the structure moving out of phase. Indeed, these two measured modes correspond to the first two vertical modes simulated by COMSOL, shown as the third and fifth mode in figure 3.6. The center of the beam at the 80 kHz mode (see figure 3.14B:orange line) shows a minimum on top of the maximum of the edges of the structure. Although this minimum is unexpected, there is no definite explanation. The minimum can not be caused by a phase step, since the wavelength is 666 nm.

Table 3.2 shows the results for the resonance frequencies of four different de-

---

[1] see: https://www.lynceetec.com/mems-analysis-tool/

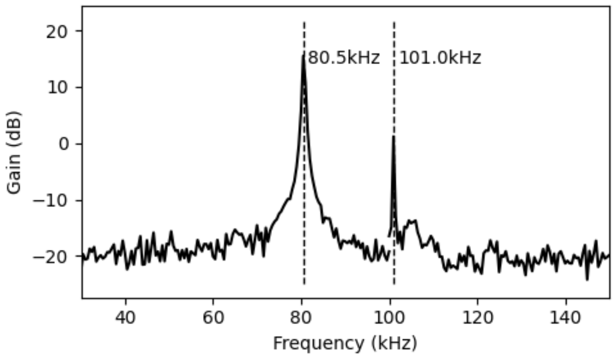

Figure 3.13: Vertical frequency response spectrum of suspended MEMS structure

vices and the COMSOL simulation results. The resonance frequencies computed by COMSOL are significantly lower compared to those obtained from measurements. However, the ratio between the first and second resonance frequency does not differ significantly. This suggests that the reason for the discrepancy between the simulation and measurements is not of due to geometrical differences, as this would affect the resonance frequencies as well as the ratio between them. The difference between COMSOL and measured resonance frequencies is a factor of roughly 1.25 for both modes. This suggests that either the mass of the resonating structure is 1.55 times lower or its stiffness is 1.55 times higher than modelled, since

$$f_0 \propto \sqrt{\frac{k}{m}} \tag{3.1}$$

A factor of 1.55 deviation for mass or stiffness from design values is not realistic. Besides, the voltage-displacement measurements were in good agreement with the COMSOL simulation. This simulation could not have been accurate if the mass or stiffness had been off by a factor of 1.55. A possible explanation for the increased resonance frequency is stiffening of the structure due to an offset voltage. However, this is not confirmed by simulations or calculations.

Other parameters of the COMSOL model that will have an impact on the resonance frequency are Young's modulus and Poisson ratio of the MEMS material. Additional simulations are done to answer the question whether the resonance frequencies are susceptible to a small deviation in the Young's modulus and Poisson ratio of the structure's silicon, but also the structure thickness. The results for the first two vertical resonance frequencies as a function of these parameters are shown in figure 3.15.

	$F_0^R\ (kHz)$	$F_1^R\ (kHz)$	F_0^R/F_1^R
Device 0	80.5	101.0	0.80
Device 1	82.0	103.0	0.80
Device 2	82.5	104.0	0.79
Device 3	81.0	100.5	0.81
Device average	81.5	102.1	0.80
COMSOL simulation	63.9	82.8	0.77

Table 3.2: First two vertical resonances of four devices measured using the Lynceetec and of the COMSOL simulation, and the ratio between them.

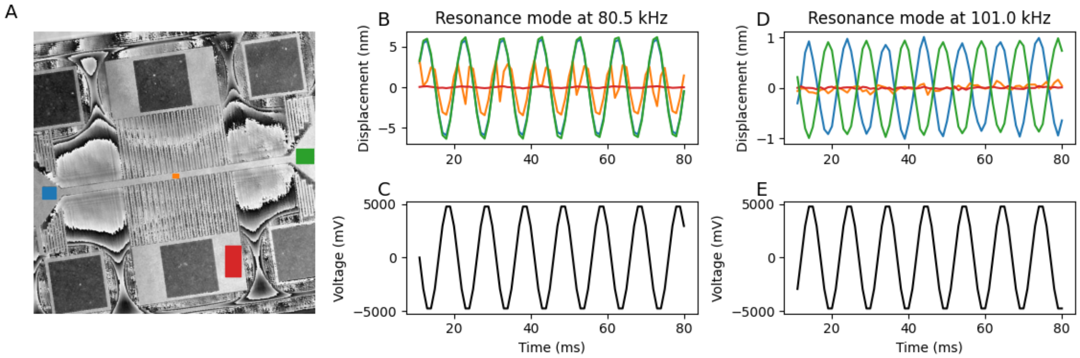

Figure 3.14: Mode shape representation of the MEMS resonances frequencies measured with the Lynceetec. **A)** shows the regions of which the average vertical position is plotted in the corresponding colors in **B)** and **D)**. **C)** and **D)** show the electrical Lynceetec output signal that is fed to the piezoelectric shaker on which the chip is put.

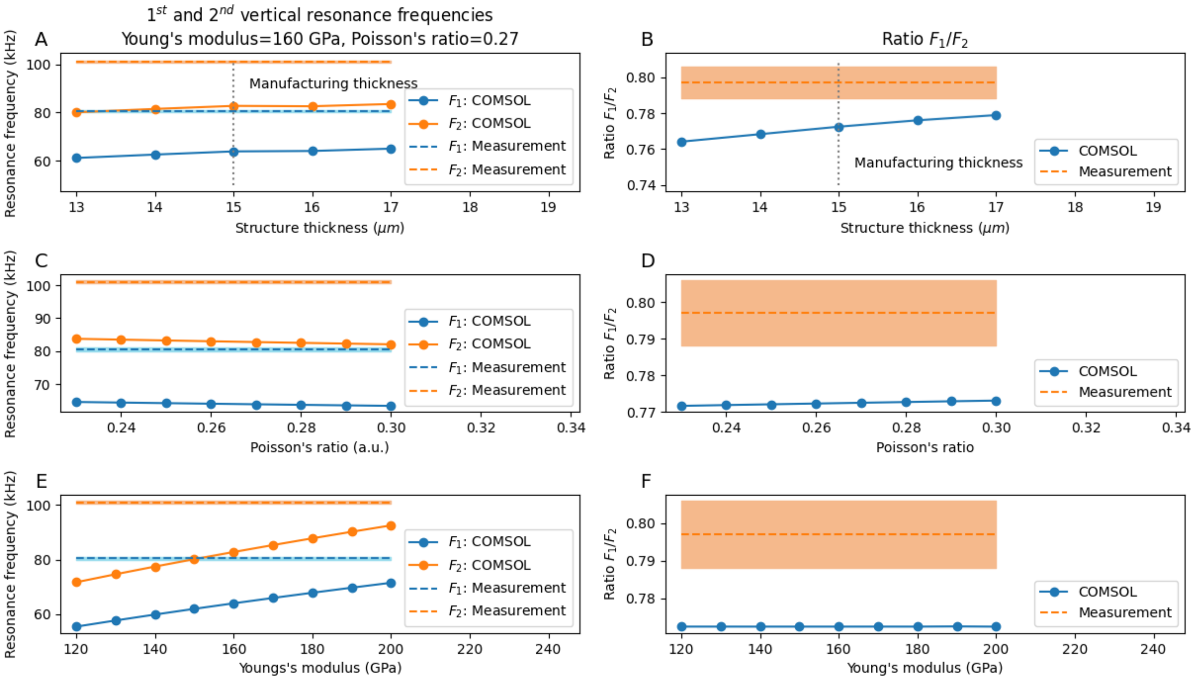

Figure 3.15: Investigation of the effect of small deviations in **A,B)** the structure thickness, **C,D)** Young's modulus and **E,F)** Poisson ratio on the first two vertical resonances frequencies, as well as the ratio between these frequencies.

The structure thickness has only a small effect on the resonance frequencies, but a significant effect on the ratio between the frequencies. However, achieving a perfect match between this ratio from simulation and measurement would require a structure thickness higher than 20 μm in the simulation. Although small deviations with respect to the design values may occur, 20 μm is too far from the design value of 15 μm. The Poisson ratio has negligible effect on both the frequencies and their ratio.

The Young's modulus has a strong effect on the resonance frequencies, but no effect on the their ratio. However, the difference between simulation and measurement cannot be explained by small deviations in the Young's modulus, since this would require the simulation to assume a Young's modulus of silicon that is above physical values. In conclusion, the difference in the first two vertical resonance frequencies between the COMSOL simulation and measurements is not due to small deviations in the structure thickness, the structure's Young's modulus or Poisson ratio. The true reason for the discrepancy remains unknown in this study.

3.7 Vertical stiffness of device

The process of graphene transfer onto the MEMS structure relies heavily on the assumption that the vertical stiffness of the suspended structure is sufficiently high. During the transfer, graphene is pressed onto the surface of the structure to make it stick. If the structure is too flexible in the vertical direction, pressing graphene onto its surface will be difficult because the structure is pushed away. To quantify the vertical stiffness of the structure, vertical force-deformation measurements were performed on the structure with a Femtotools FT-NMT03 Nanomechanical Testing System. This system precisely controls the movement of a microneedle while accurately measuring the force on the needle. The needle, a silicon needle with a flat, square tip of size 50 μm by 50 μm, was positioned perpendicular to the surface of the structure on a distance of 10 μm. Since the silicon substrate beneath the structure has a finite stiffness, a calibration measurement was performed on the edge of the chip to determine the substrate stiffness. In subsequent measurements, this substrate stiffness is automatically subtracted by the Femtotools monitoring software.

The force-deformation graphs show two regimes for the vertical stiffness, see figure 3.16A and 3.16B. The stiffness in the first regime is roughly $\sim$165 N/m and in the second regime $\sim$2650 N/m. The COMSOL simulation shown in figure 3.16D gives a vertical stiffness of 205.3 N/m, which is close to the stiffness in the first regime. The reason for the small difference can be that in the COMSOL simulation the stiffness is calculated using a uniform load on the full surface of the suspended structure, while the measurement was done with local force. Using a local force on one side of the structure will lead to tilting of the device, such that the structure will deform more on the side where the force is applied and less on the other side. This will result in a lower stiffness when using a local force compared to homogeneous loading of the structure. The COMSOL simulation does not show another regime with higher stiffness. The reason for the transition to the stiffer regime could be that the structure is touching the edge of the cavity or the back gate located beneath. The low vertical stiffness of the structure can cause problems with the transfer of graphene, if the pressure required to make the graphene stick is high compared to the stiffness of the suspended structure.

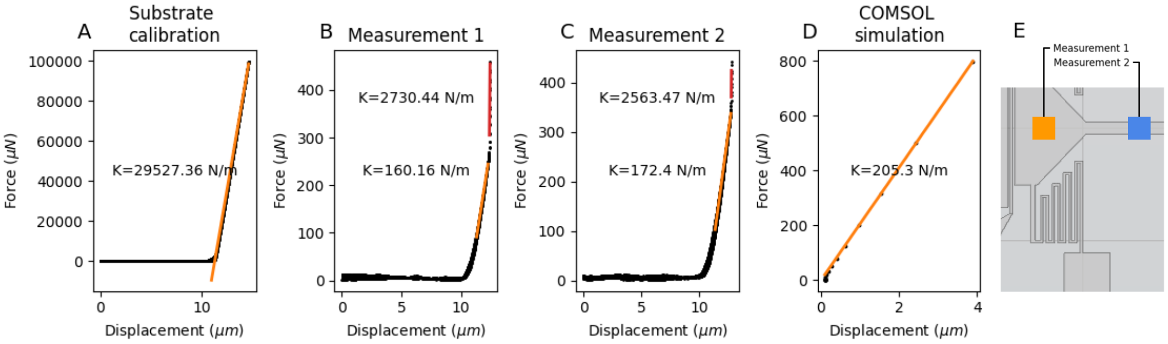

Figure 3.16: Femtotools force-deformation measurement on **A)** the silicon substrate for calibration for substrate stiffness, **B)** and **C)** two different positions on the suspended structure. **D)** shows The two measurement positions of **B)** and **C)** are shown in **E)**.

Chapter 4

MEMS measurements

4.1 Sample preparation

Once the behavior of the MEMS device is understood, the next step is to transfer graphene onto the structure. There are different methods for graphene transfer, divided into wet and dry transfer methods. Wet methods often involve placing the sample in liquid, for instance to pick up a flake of graphene floating on the liquid [46] or to dissolve a polymer that is supporting the graphene [50]. For the MEMS device used in this study, drying the structure after submerging in liquid will cause stiction of the fingers. Since surface adhesion forces are relatively strong in the MEMS device, it is difficult to get the fingers loose when they are stuck together without damaging the device. Avoiding the problem of stiction due to evaporation of liquid requires critical point drying (CPD). Because CPD is a time-consuming and difficult process when using the machine available in this study, wet transfer and subsequent CPD will only be used as a last resort. Initially, a dry method will be used to transfer graphene to the MEMS device.

Mechanical exfoliation using the Scotch tape method is used to make thin flakes of graphene, ranging in size between microns to tens of microns and with thickness of nanometers to tens of nanometers. Figure 4.1A shows the setup used for graphene transfer. The setup consists of a positioning stage with precise position control in three directions, but also control over the tilt of the attached glass slide in two directions. The sample onto which graphene has to be transfered is fixed on a heater stage. The sample is fixed by placing it on a hole and creating a vacuum in the hole below the sample. Above the sample, there is an overhead microscope with long working distance objectives of 5x, 10x and 20x magnification. The vertical position of the objective head can be adjusted to bring the sample into focus. The stamping process consists of multiple steps, shown in figure 4.1B. The steps are described in detail below:

1. Place a piece of graphite in between to pieces of Scotch tape and pull

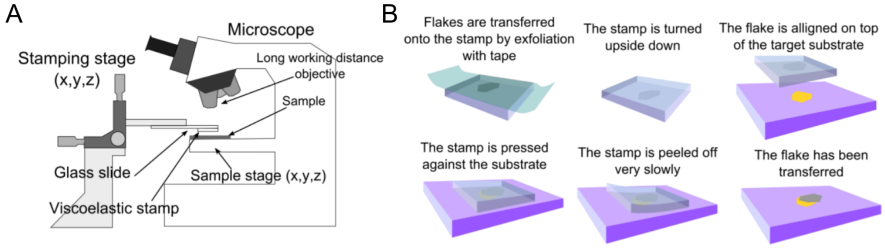

Figure 4.1: **A)** graphene transfer setup, consisting of a positioning stage with an overhead microscope. **B)** mechanical exfoliating method using Scotch tape and a polymer stamping substrate. Figure taken from [51].

them apart. Flakes of graphite will stick to both sides of the tape. Put a clean piece of tape on one of these flakes and pull the tape apart again. Repeat the process until the graphite is broken down to small, thin flakes of graphene.

2. Put a small square (∼0.5 by 0.5 cm) of polymer substrate on a glass slide. Remove trapped air bubbles by applying pressurized air or gently squeezing them out using tweezers.

3. Put the tape with graphene onto the polymer substrate. Ensure that the tape makes good contact with the polymer, press gently on the tape with a flat object if necessary. Tear off the tape from the polymer with a quick stroke. The quicker the tape is pulled of, the higher the change that the graphene sticks.

4. Use a microscope to inspect the graphene that has been transfered to the polymer substrate. The color of the flakes relative to the background is an indication of the thickness of the flake. Since the substrate and glass slide are highly transparent, it is convenient to put a piece of silicon below the glass to provide good contrast. If the color of the flake is similar to the silicon, the flake is thin. If the color of the flake is white, the flake is very thick. Choose a flake that is thin and large, but without tears and cracks.

5. Attach the glass slide to the positioning stage with the polymer substrate on the bottom side. Move the positioning stage such that the flake is directly above the target location on the sample.

6. Lower the positioning stage to bring the polymer in contact with the sample. A contact line will become visible, indicating where it is touching the sample and where it is not. While pushing down, the contact line will move across the sample. Ensure that the flake is in contact with the sample, meaning the contact line should have moved over the flake. The

displacement direction and angle of the contact line can be controlled by adjusting the tilt of the positioning stage before bringing the polymer into contact with the sample.

7. Slowly peel off the polymer substrate by lifting the positioning stage. The slower the polymer is peeled off, the higher the change that the flake will stick to the sample. A method that can be used to peel very slowly and continuously is by using the heater stage. Heating the stage will heat the sample, which expands and thereby makes contact with the polymer. In order to peel the polymer off, let the sample shrink by cooling it down. The peeling speed is determined by the cooling rate, which depends on the temperature difference between the sample and the environment. The peeling speed can thus be controlled by adjusting the maximal temperature of the sample.

The transfers for this study are done in a cleanroom to minimize contamination of the sample. The substrate used for stamping is PDMS, with a thickness of 1-2 mm. It is important to be aware of the fact that the tape may leave adhesive on the flake. The amount of adhesive left on the flake depends strongly on the brand of tape. For this study, the degree of substrate contamination by adhesive is compared using an optical microscope and the brand with lowest contamination is used for the rest of this study.

One challenge of the transfer process described above is to avoid the situation where the substrate touches a large area of the sample. In principle this is not necessary when the target flake on the polymer substrate is close to the edge and the target location on the sample is close the the edge. However, both these factors are can not be controlled during the transfer process. The problems with the polymer touching a large area of the sample are the unwanted transfer of other flakes from the substrate and the contamination of the sample contact area with tape adhesive and polymer residual. The risk of contamination the sample with graphene, polymer or adhesive can be reduced by minimizing the contact area between polymer and sample. This can be achieved by using a PDMS dome or droplet, rather than a flat film. When using a PDMS dome, the contact area will be local and circular, with its diameter depending on the diameter and curvature of the dome and compression of the dome by the stamping force.

The complex structure of the MEMS device causes multiple difficulties in the transfer process. In the first place, the material needs to be transfered over a trench. This is more challenging than transferring on a simple drum (see figure 4.2A and 4.2B), because part of the edges of the flake do not adhere to the silicon. When peeling off the substrate, these edges remain attached to the polymer substrate at almost every attempt and pull off the rest of the flake when the polymer is retracted. In order to improve the success probability of transferring graphene over a trench, a thin polymer film was added on top of the substrate. This polymer PPC becomes softer and more viscous upon heating

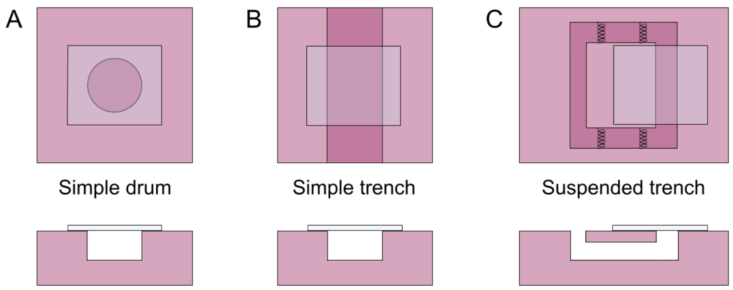

Figure 4.2: Flake of graphene on top of a **A)** simple drum, **B)** simple trench and **C)** trench with a suspended edge.

Figure 4.3: **1-3)** peel the spin coated film of PPC from the cover slide using a rectangular window of Scotch tape. **4-5)** attach the tape window to the glass slide such that the film covers the PDMS substrate.

in the range till 100°C, which reduces its surface adhesion. Above 100°C, PPC changes from a viscous film into a fluid. The reduction of surface adhesion can be used to release the graphene from the substrate, as was shown in [52]. PPC is a transparent polymer, which is an important requirement for the polymer substrate in order to view to flake through the substrate.

In this study, PPC films are made by dissolving granular PPC in anisole with mass ratio of 15%:85% and spin coating it on a cover slide. After 15 minutes, the film is be removed from the cover slide using Scotch tape, see figure 4.3A-C. The result is a rectangular film spanned across a window of tape. This window can be put onto the glass slide, with the film covering the PDMS substrate, either dome or film, see figure 4.3.C,D. The tape window should be attached such that the PPC film is not wrinkled close to the top of the dome and is under slight tension. It is convenient to cut away the excess tape, since excess tape covering the bottom of the glass slide deteriorates the image quality when imaging through the glass slide and substrate.

In order to transfer graphene using the PPC film, some additional steps are necessary. The full process is described below:

1. Transfer a flake of graphene onto a bare silicon chip using only PDMS, following the description given above.

2. Stamp the PDMS with PPC film onto the flake, which is on the bare silicon chip. Heat the chip to 30 °C and let is cool again. This allows the PPC to adhere to the flake strong enough to peel if from the silicon.

3. Retract the substrate and replace the bare silicon chip with the sample. Position the flake above the target location on the sample and push it down so that the substrate makes contact with the sample.

4. Heat the sample to 70°C, which makes the PPC more viscous and less adhering to the flake.

5. Once the sample is 70°C, retract the PDMS with PPC slowly. The graphene should stick to the sample and the PPC should not leave any residue on the sample.

For testing purposes, graphene is transfered over a simple trench in a bare silicon chip. Although transferring over this trench with bare PDMS is difficult and has a low success rate, using PDMS with PPC film the transfer is much easier and success rate improves to almost 100%. In addition to transferring over a trench, this method provides a tool for pick-and-place of flakes on silicon chips, which is useful in many applications. However, it should be noted that repeated cycles of pick-and-place of a single flake easily introduces corrugations in the flake, such as folds and tears.

The next step is to try the transfer on the MEMS device, which is a trench with one edge being suspended, see figure 4.2C. This poses the additional problem that part of the stamping surface moves in the vertical direction when force is applied. Although the suspended structure is strong enough not to break during transfer, its vertical displacement is a major problem for the transfer. Figure 4.4 shows an illustration of the peeling effect due to the vertical displacement of the suspended structure. Figure 4.5 shows microscope images that are made during the transfer process, where the region of the flake with colored fringes is not touching the surface of the MEMS. It is clear that the peeling of the flake from the sample starts at the edge of the trench. The pulling up of the suspended structure while retracting the substrate is due to surface adhesion between the polymer substrate and the silicon. Despite the PPC surface adhesion decrease upon heating, a PPC film on top of the PDMS dome does not solve the problem. Different people together have spent multiple weeks trying the graphene transfer onto the MEMS devices, using both PDMS domes and flat PDMS covered with PPC film, without success. Plasma cleaning and oxidation are performed to make the sample surface more hydrophobic, thus increasing the adhesion with graphene, but neither improves the transfer process.

Another factor that appeared problematic during transfer is the high surface roughness of the MEMS surface. This is confirmed by the observation that transferring graphene onto a flat area of the chip is significantly harder compared to transferring to a bare silicon chip, with the only difference being the surface

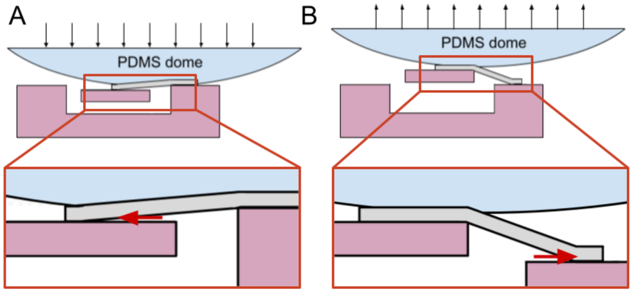

Figure 4.4: **A)** while pushing the suspended structure down during stamping, or **B)** while pulling the suspended structure up after stamping, the height difference between both edges of the trench creates a peeling effect on the graphene at one of the trench edges.

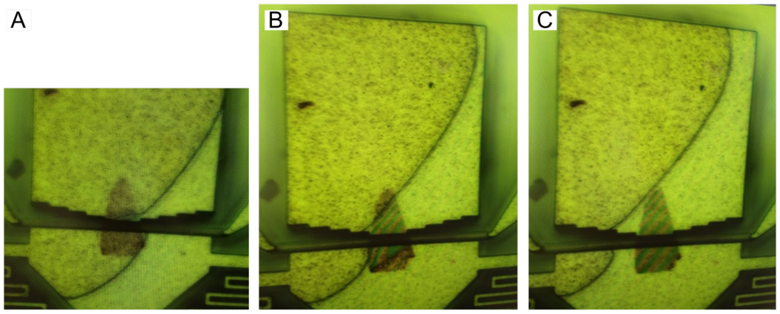

Figure 4.5: Three stages during the substrate retraction process showing the peeling off of the flake. The part of the flake showing colored fringes is not touching the surface anymore.

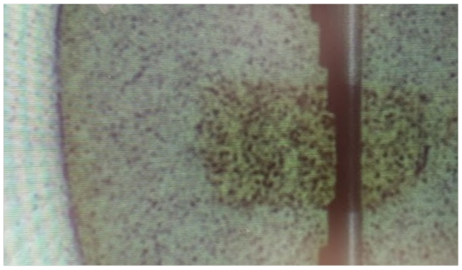

Figure 4.6: Microscope image of the sample during the transfer process, with the contact line visible on the left, the substrate touching the sample on the right of this line and a flake of graphene with air trapped underneath.

roughness. The MEMS surface is etched by X-FAB using a coarse etching method, without smoothing the surface afterwards. The roughness of the surface results in poor adhesion between the graphene and the structure. This is visible in figure 4.6 as the appearance of black spots, which are air bubbles trapped in between the graphene and the surface. When pushing the substrate on the sample very slowly, some air bubbles disappear was the air is squeezed out. However, a large fraction of the bubbles remain when pushing on the substrate with considerable force. Most likely, these bubbles are trapped in a hole in the surface, with graphene sealing this hole from above. The graphene often starts peeling off at black spots which are near the edges of the flake. Therefore, the surface roughness likely is a significant factor in the experienced difficulties with graphene transfer.

One way of improving the transfer process is to increase the adhesion between graphene and the MEMS surface by smoothing the MEMS surface. Reducing the surface roughness can be done by removing the peaks or filling the holes. A 100 nm thick gold sputter coating is added on top of the MEMS surface in an attempt to fill the holes. Figure 4.7 shows AFM measurements of the MEMS surface before and after gold coating. Surprisingly, the RMS roughness of the surface increases after gold sputter coating by almost a factor of two, from 19.5 nm to 30.7 nm. The reason for the roughness increase is that the sputtering method used sputters gold particles moving in random direction, so that their trajectory is not necessarily perpendicular to the sample plane. Gold particles that collide onto the surface at an angle are more likely to land on a peak than in a hole, because the peaks create shadows where no gold particles will land. These coating shadows will increase the roughness. Adding a gold coating on the MEMS surface is not the solution for the transfer problems. Gold sputter coating was performed by Roberto Pezone, Msc and AFM measurements were done by Niels Bouman, BSc.

Plasma oxidation and vapor HF etching are performed as an attempt to remove the peaks on the MEMS surface. Vapor HF etches away SiO_2 but not

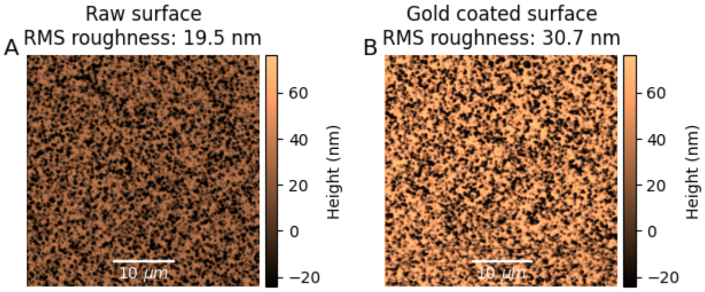

Figure 4.7: AFM measurement of **A)** the raw and **A)** the 100 nm gold coated MEMS surface

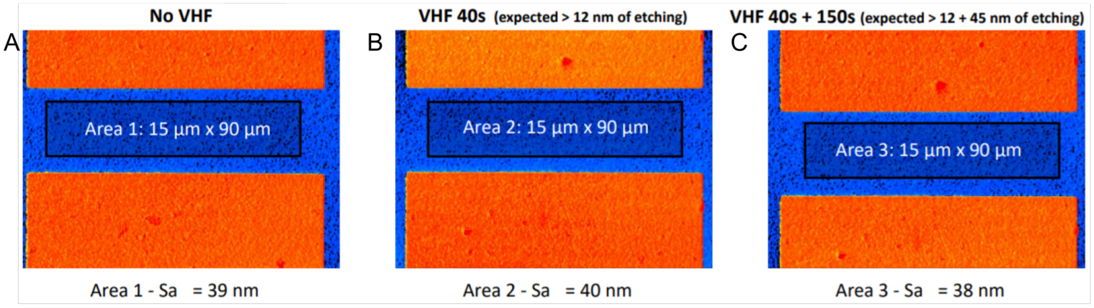

Figure 4.8: 3D Laser Scanning Confocal Microscope images of MEMS surface **A)** without vapor HF etching, **B)** after 40 seconds and **C)** after 190 seconds of vapor HF etching. The value Sa denoted below each figure is the arithmetic mean height of the corresponding area. Measurements done

Si. A layer of SiO_2 is created on the MEMS surface using plasma oxidation. Since this layer of oxide forms approximately 50% inside and 50% outside of the silicon, the oxide layer will smooth the silicon layer underneath. Vapor HF treatments are performed for 40 and 150 seconds. Since the etching rate is 0.3 nm per second, this means that 12 nm and 57 nm of oxide are removed in total after the first and second treatment respectively. Figure 4.8 shows 3D laser scanning confocal microscopy images of the MEMS surface without vapor HF treatment, after 40 and 190 seconds of vapor HF treatment. The arithmetic mean height Sa of the surface, which is a measure for surface roughness, does not change after the vapor HF etching. It is possible that the reduction in surface roughness is below the optical detection limit. This suggestion is supported by the fact that oxidation and etching will only reduce roughness locally, on a typical length scale of half the oxide thickness.

Figure 4.9 shows the theoretical smoothing of the MEMS surface after re-

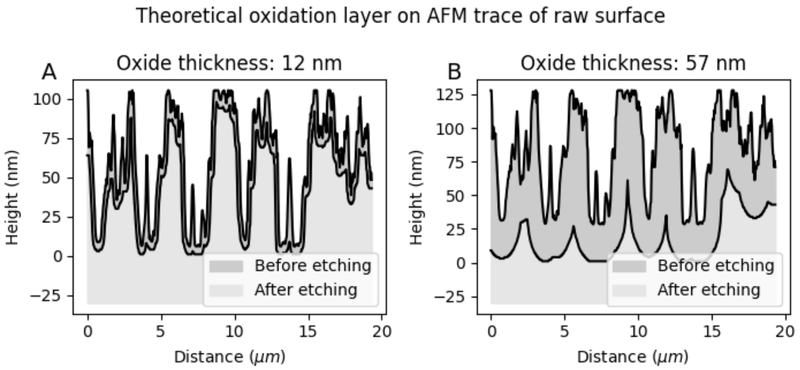

Figure 4.9: Theoretical oxide layer calculated for an AFM trace of the raw MEMS surface for **A)** an oxide layer of 12 nm and **B)** an oxide layer of 57 nm.

moving 12 and 57 nm of oxide. After removal of 57 nm of oxide, the surface roughness has decreased significantly. Since this significant decrease is not visible in 3D laser scanning images after vapor HF treatment, it is possible that the oxide layer on the chip was only a few nm thick. Since there is no method available to measure the oxide thickness, this hypothesis cannot be confirmed. Plasma oxidation does not easily create a thick layer of oxide. A thick oxidation layer can be made by thermal oxidation. Because the MEMS device cannot endure high temperatures, thermal oxidation is not an option in this case. Oxidation and etching steps have not improved the transfer process. 3D laser scanning confocal microscope measurements and vapor HF etching were performed by Roberto Pezone, MSc. Plasma oxidation was performed by Niels Bouman, BSc.

Different parameters of the transfer process are varied to optimize the process. The parameters are thickness of the flake, curvature of the PDMS dome, temperature of the stage (60 °C to 100 °C), speed of substrate peeling and the angle of substrate peeling. Although each of these parameters effects the transfer process, none of them provides the solution to the transfer problem. A different approach that is tried is to melt the PPC completely, so that it remains on the sample together with the flake. Afterwards, the PPC can be evaporated by baking in an oven at ∼180 °C.

By melting the PPC film with graphene on top, it was possible to put the flake of graphene onto the target location on the sample, see figure 4.10B. The transfered flake was sagged heavily, which is not desirable in experiments. Figure 4.10A shows that melting the PPC caused the comb fingers to stick together, which is due to viscous forces of the molten PPC. Figure 4.10C shows that baking the PPC at 180 °C does indeed remove the polymer. However, it is unclear whether all PPC can be removed from the flake itself, from underneath

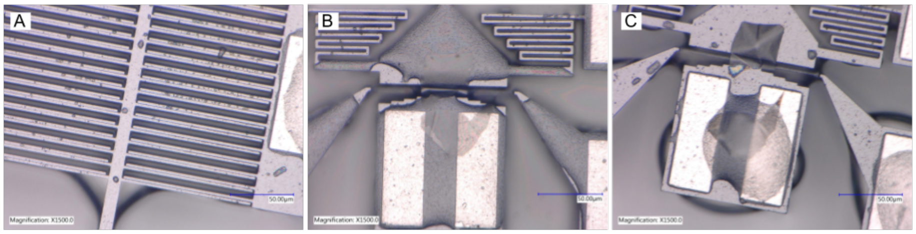

Figure 4.10: **A)** and **B)** show optical images of the MEMS structure directly after heating the sample to 120 °C during transfer, which melts the PPC. The comb fingers are stuck together due to viscous forces of the molten PPC. **C)** shows an optical image of the MEMS structure after 30 minutes of baking at 180 °C

the structure and from in between the stuck comb fingers. After baking the PPC off, the comb fingers remain stuck, as is expected. Although it is possible to push the fingers loose when they are stuck using a probe needle, this requires considerable force. Displacement and vibrations of the suspended part due to this force would likely break or collapse the suspended membrane.

The final parameter that can be varied is the 2D material itself. Because all materials have unique surface interactions with the silicon dioxide on the MEMS surface, it is well possible that another 2D material can be transfered more easily. The 2D material molybdenum disulfide (MoS_2) is used for transfer as alternative for graphene. Although transfer with MoS_2 is not significantly easier, it seems that MoS_2 sticks to the surface of the MEMS device better. After attempting the MoS_2 transfer for multiple days, one flake is transfered to the MEMS device. This successful transfer required a portion of luck, since the flake teared apart while peeling off the substrate, leaving a small piece of MoS_2 on the sample. The MEMS device with a flake of MoS_2 on top is shown in figure 4.11. Figure 4.12B shows a Lynceetec measurement of the MoS_2 flake. The difference in average height between the two rectangular areas shown in figure 4.12A is 30.97 nm. This means that the flake is approximately 45 layers thick.

4.2 Force-displacement measurements

Since the result of the COMSOL simulation is in good agreement with the characterization measurement (see figure 3.11), the simulation results are used to find the relation between voltage and force. This is possible because the stiffness of the device is measured using a boundary load and using a voltage across the fingers, thereby uncoupling the electrostatic force from the spring force. The boundary load simulation gives a displacement of the structure, as well as a comb-drive voltage. The comb-drive voltage can thus be related to

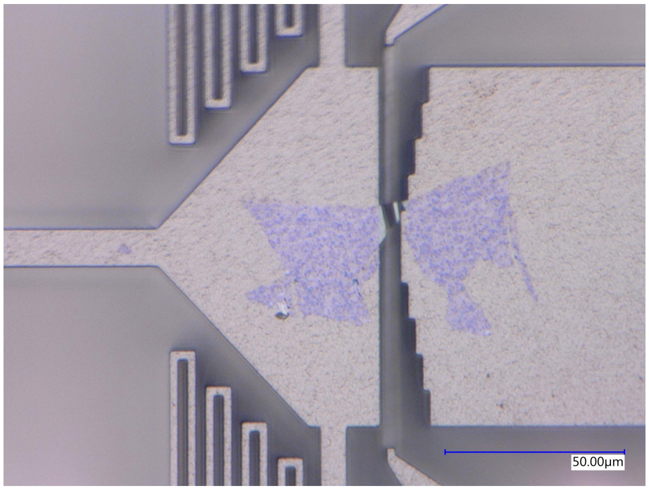

Figure 4.11: MEMS device with flake of MoS_2 spanned over the trench.

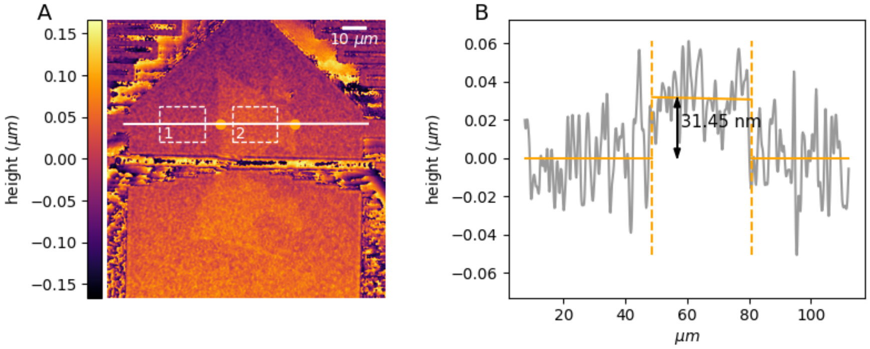

Figure 4.12: **A)** Lynceetec measurement of the MoS_2 flake on the device. **B)** shows a plot of the profile along the white line in **A)**.

the equivalent boundary load via the displacement of the structure. Figure 4.13 shows the force-displacement curves for the COMSOL simulation, characterization measurement and the measurement on the MoS_2 flake. The stiffness value determined from the characterization measurement, 125±5 Nm^{-1}, agrees with the estimated stiffness value and is close to the value of the COMSOL model.

The force-displacement curve of the MoS_2 measurement shows two different regimes, distinguishable by the stiffness. In the first regime, the stiffness of the structure including the flake has increased by roughly 60%. The stiffness of the flake can be calculated by modeling the flake as a spring in parallel with two MEMS springs. This parallel system of springs in turn is in series with another parallel system of two MEMS springs. The total spring constant is given as

$$k_{\text{total}} = \left((k_{\text{spring}} + k_{\text{spring}})^{-1} + (k_{\text{spring}} + k_{\text{spring}} + k_{\text{flake}})^{-1}\right)^{-1} \tag{4.1}$$

where k_{flake} is the stiffness of the flake. Considering the stiffness $k_{\text{total}} = 245 \pm 70$ Nm^{-1} found from the measurement, the stiffness of the flake must be 1660 ± 484 Nm^{-1}. The Young's modulus of MoS_2 is 270 ± 100 GPa [53]. The Young's modulus is converted into a stiffness using the formula

$$k = \frac{EA}{L_0}, \tag{4.2}$$

where E is the Young's modulus, A is the area of a cross section perpendicular to the applied force and L_0 is the initial length of the membrane in the direction of the applied force. Using that the flake is roughly 6 μm wide at the smallest point, the thickness is 30 nm and the initial width of the trench is 6 μm, the stiffness of the flake is expected to be 8100 ± 3000 Nm^{-1} based on the Young's modulus reported by [53]. This value is four times higher than the measured flake stiffness. The reason for this difference can be the wrinkles in the flake, as shown in figure 4.14B.

For forces above 20 μm, the stiffness of the structure drops almost one order of magnitude. It is likely that the flake teared, softening the structure in the second regime. The stiffness in the second regime is lower than the stiffness of the empty device, but the cause of this could not be determined. The total strain created by the MEMS device is 6.6%, but the flake has likely teared at a strain of roughly 1.7%.

In order to study the wrinkles in the flake, an average profile is taken over the rectangular area shown in white in figure 4.14A. The average profile is shown in figure 4.14B. The right part of the profile, starting at 10 μm, is not affected by voltage. This is as expected, since this region corresponds to the fixed edge of the trench. The flake exhibits some wrinkles, visible in figure 4.14B. In order to quantify the effect of voltage on the wrinkles, the RMS surface roughness is determined, as shown in figure 4.14C. The RMS surface roughness has a

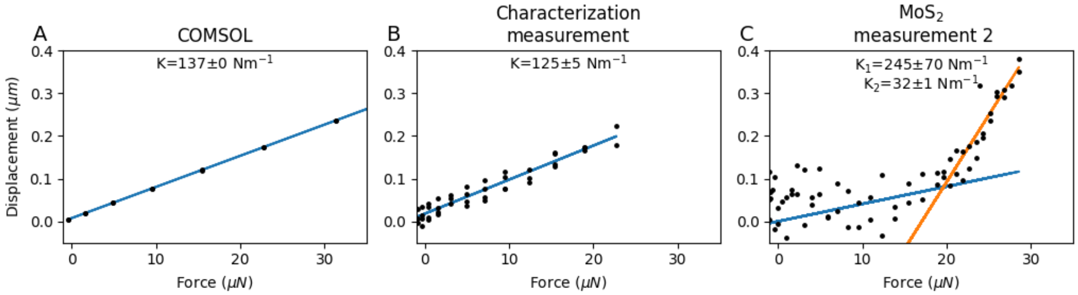

Figure 4.13: Force-displacement curves for **A)** the COMSOL model, **B)** the characterization measurement and **C)** the measurement with the MoS$_2$ flake on the device. In each graph, the stiffness value corresponding to the linear fit is shown.

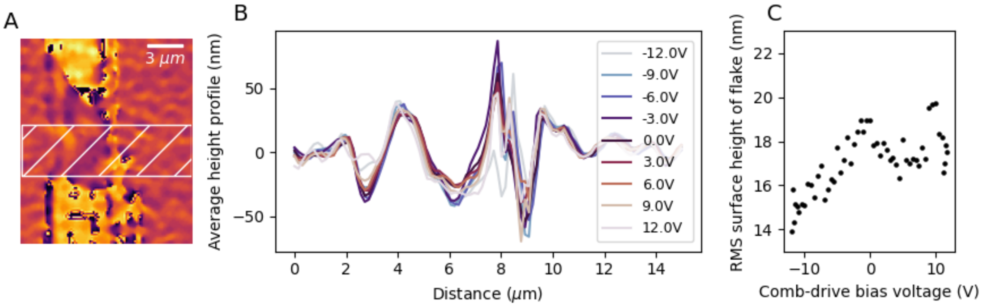

Figure 4.14: **A)** region of interest around the MoS$_2$ flake, at 0.0V. The profile, averaged in vertical direction over the white hatched rectangular region is shown in **B)** as a function of comb-drive voltage. **C)** RMS surface roughness of the white hatched area in **A)** as a function of comb-drive bias voltage.

maximum at 0V and decreases with increasing comb-drive bias. This shows that pulling on the flake flattens the wrinkles. However, the maximal strain applied in this experiment is not enough to remove all wrinkles from the flake, since the RMS surface roughness decreased only by 25% at -12V. This explains why the stiffness of the flake is lower than the expected value based on the Young's modulus of MoS$_2$. For high positive bias voltages, the RMS surface roughness increases. This is likely a consequence of the tearing of the flake.

4.3 Conclusion and discussion

The concept of force-displacement measurements using MEMS devices with a 2D membrane on top is a promising method for measuring membrane properties. However, in this study several factors are encountered that make it difficult to do good experiments. In the first place, using the described methods is is practically impossible to transfer a flake of either graphene or MoS_2 onto the MEMS device. For this reason, it is not possible to do any measurements on graphene or to do multiple measurements or prove repeatability for the measurement with the single MoS_2 device. The transfer is challenging because the flake needs to be stamped over a trench, of which one edge can move vertically. Also the high surface roughness of the MEMS makes it difficult to bring the flake in good contact with the surface. Different attempts are made to improve the transfer process by reducing the surface roughness, such as oxidation, vapor HF etching and gold sputtering. Since none of these attempts improves the surface significantly, the transfer process remains very challenging.

Further attempts on improving the transfer process could focus on improving the adhesion between graphene and the substrate, for instance by controlling humidity, surface hydrophobic or adding a sticky layer such as HDMS. Another attempt could be made at melting the PPC onto the chip together with the flake and bake the PPC off. This needs to be done in a more controlled manner than was done in this study, to prevent stiction of the comb fingers. More aggressive smoothing of the MEMS surface could also help, however this does not solve the challenge of the vertical movement of the suspended comb and will therefore likely not be sufficient for successful transfer. As a last option, wet transfer can be considered. This will require CPD, since stiction of the fingers will likely happen when the MEMS is taken out of liquid. In the ideal situation, the suspended comb would not be suspended during transfer. This can be achieved by etching away the oxide after the transfer step. Because the batch of chips is ordered from a commercial foundry, it is not possible to change the order of transfer and oxide etching now. In future projects, it would be beneficial to take the transfer process into account already during manufacturing of the MEMS.

The single MoS_2 device that is made is the result of the only successful transfer onto a MEMS device during this study. For this device, the stiffness of the flake was determined to be 1660 ± 484 Nm^{-1}, which is four times lower than the theoretical stiffness of the flake. The force-displacement curve shows two regimes, where the first regime is stiff because of the flake, but the second regime is less stiff, even softer than the empty device. The reason for the softening of the structure likely is tearing of the flake. However, the fact that the stiffness after tearing of the flake is lower than that of the empty device cannot be explained. Because of the aforementioned problems with the transfer process, it is impossible to repeat the experiment and investigate this observation in more detail. Analysis of the flake surface shows that the wrinkle pattern does not change significantly upon increasing comb-drive bias voltage. The RMS surface roughness of the flake decreases with increasing comb-drive bias, but only with 25% and without clearly visible effect on the wrinkles.

The experiments show that the method of multiwavelength interferometry provides sufficient lateral resolution to determine the MEMS displacement with enough accuracy to extract information about the suspended 2D membrane. It is also possible to monitor the surface topology of the suspended membrane. This shows that the monochromatic or multiwavelength interference method used in this study is suitable for investigating the phenomenon of wrinkling with the aid of a MEMS device for strain engineering. Because of its non-invasive nature and high vertical resolution, optical interference is promising for future research on membrane topology.

Because the challenge of transfer of membranes cannot be solved in this study due to time limitations, a different route will be explored for studying the effect of strain on wrinkles in graphene. An alternative to MEMS straining is to make use of suspended drums chip with a back gate to electrostatically strain the membrane. This route will be followed in the remainder of this study.

Chapter 5

Drum deflection measurements

5.1 Drum deflection measurements

Pulling on a membrane that is suspended on a hole is an alternative method to induce strain. This method is a common way to determine properties of thin films and referred to as the bulge-test method. There are different methods to deflect a suspended drum; gas pressure [28], nanoindentation [54] and electrostatic pressure [55]. In this study, electrostatic pressure will be used to deflect a graphene drum. Since graphene is a zero bandgap material, it is a conductor. With a backgate beneath the graphene drum, the conducting drum will act as a capacitor. In a charged capacitor, there are electrostatic forces between the opposing surfaces. The graphene drum will be pulled towards the backgate by this electrostatic force. This deflection of the drum causes straining of the membrane.

For a thick membrane, out-of-plane deflection requires both bending energy and stretching energy. However, thin membranes have a negligible bending energy compared to their stretching energy. For such thin membranes, out-of-plane deflection only requires stretching energy, which implies that the Young's modulus determines the relation between pressure and deflection. The Young's modulus and pre-stress of a thin membrane can be found by fitting the experimental pressure-deflection data [56] with the bulge-test equation

$$P = 4\frac{\sigma_0}{a^2}h + \frac{8E_{2D}}{3(1-\nu)a^4}h^3, \tag{5.1}$$

where P is the pressure, σ_0 is pretension, t and h are membrane thickness and center deflection. In experiments, the voltage rather than the pressure is a control parameter. Therefore, the pressure P needs to be expressed in terms of voltage V. Here the drum will be treated as a parallel plate capacitor. This approximation is valid if the membrane and backgate are flat and parallel and the distance between the membrane and gate is small compared to the overlap area of membrane and gate. These approximations require that the deflection of the membrane is small compared to the distance between membrane and gate, $h_V(x,y) << d$. Since this distance d is 10 μm and the maximal deflection is roughly 750 nm, this condition is satisfied. The drum capacitance is then given as

$$C = \frac{\kappa\epsilon_0 A}{d} \tag{5.2}$$

The electrostatic force on the membrane in the parallel plate approximation is

$$F_e = -\frac{\partial U_e}{\partial d} = -\frac{\partial}{\partial d}\left(\frac{1}{2}CV^2\right) = -\frac{\partial}{\partial d}\left(\frac{\kappa\epsilon_0 A}{2d}V^2\right) = \frac{CV^2}{2d}, \tag{5.3}$$

where C is the capacitance of the drum, V is the voltage across the membrane and backgate, κ is the relative dielectric strength, ϵ_0 is the vacuum permittivity, A and a are the area and radius of the drum and d is the distance between the membrane and the backgate. The electrostatic pressure is the electrostatic force divided by the membrane area,

$$P = \frac{F_e}{\pi a^2} = \frac{CV^2}{2\pi d a^2} \tag{5.4}$$

From geometrical calculations, the radial stress σ_r and strain ϵ_r in a circular membrane are given as [56]

$$\sigma_r = \frac{Pa^2}{4ht} \tag{5.5}$$

$$\epsilon_r = \frac{2h^2}{3a^2} \tag{5.6}$$

The second way of calculating the Young's modulus is using the stress-strain relation using the expression

$$E_{2D} = (1-\nu)\frac{d\sigma}{d\epsilon} \tag{5.7}$$

5.1.1 Sample preparation and measurement

The drums for the deflection measurements are made from CVD graphene. The CVD graphene drums are manufactured by MSc. Roberto Pezone. The CVD graphene was grown on a layer of Molybdenum (Mo). Mo has a thermal expansion coefficient that is close to that of graphene, which results is less wrinkling during the cooling step of CVD compared to graphene grown on copper [57] or nickel [58]. Mo also has a low solubility of carbon, which facilitates graphene growth.

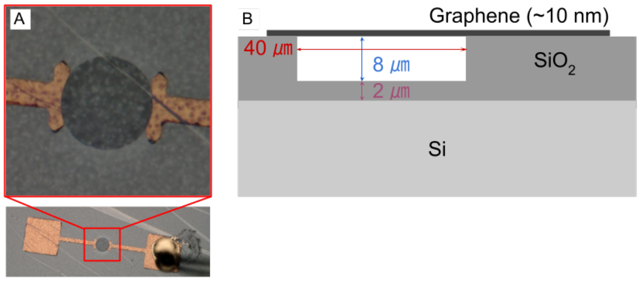

Figure 5.1: **A)** optical image of the drum, with the gold electrodes and wire bond, **B)** cross section of the silicon chip with a graphene drum.

The first step in the manufacturing process is to sputter a 50 nm thick layer of Mo on a Si/SiO_2 wafer surface. Then graphene is grown on top of the Mo layer at 915 °C. After depositing the graphene, the Mo layer is removed by submerging the wafer in a bath of hydrogen peroxide, which etches away the Mo. As the Mo is being etched away, the graphene startd to float on the liquid. After 25 minutes in 30% hydrogen peroxide solution, the solution is replaced with deionized water three times to wash away all hydrogen peroxide. The last step is to pick up the floating graphene on a target substrate. The substrate onto which the graphene is picked up is a chip with a Si bottom and a 10 μm top layer of SiO_2. In the SiO_2 layer, holes are etched of 8 μm deep with a diameter of 40 μm, over which the graphene is suspended after picking it up, see figure 5.1. More details about the CVD process can be found in [30]. Figure 5.1 shows a wire bond connected to one of the gold electrodes underneath the graphene. The silicon bottom of the chip, which acts as backgate, is attached to a chip carrier using conductive silver paint.

The thickness of the graphene is analyzed by monochromatic interferometry using the Lynceetec. Figures 5.2A,B show optical and interferometric images of a region of the sample where part of the surface is not covered with graphene. The bright yellow area in figure 5.2B is a fold in the graphene, that formed during picking up the floating flake from the liquid. Figure 5.2C shows a surface height distribution of the interferometric image. By fitting Gaussian functions to each peak, the thickness of the flake and fold are determined. The flake and fold are respectively 15±9 nm and 115±6 nm thick. The thickness uncertainty is given by the standard deviation of the Gaussian fit. The standard deviation in the peak of the substrate is three times lower than that of the flake. This means that either the flake has a non-uniform thickness or the flake does not adhere to the surface perfectly.

The capacitance of the drum follows from the parallel plate approximation, where

$$C = \frac{\kappa\epsilon_0 A}{d} = \frac{\kappa\epsilon_0 \pi a^2}{d} \tag{5.8}$$

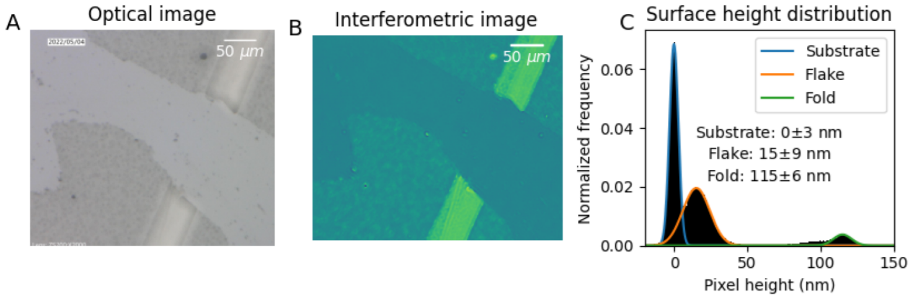

Figure 5.2: **A)** optical and **B)** interferometric image of the CVD graphene on a Si/SiO$_2$ substrate, visible in the middle. The thicker part (most yellow) of the flake is a fold. **C)** distribution of height values in the interferometric image, with Gaussian fits to determine the thickness of the flake and fold, as well as the standard deviation which is a measure of the thickness accuracy.

Since the volume in between the backgate and the membrane consists partly of air and partly of SiO$_2$, the total capacitance is

$$C_{\text{total}} = \left(\frac{1}{C_{\text{air}}} + \frac{1}{C_{\text{ox}}}\right)^{-1} = \left(\frac{d_{\text{air}}}{\kappa_{\text{air}}\epsilon_0 A} + \frac{d_{\text{ox}}}{\kappa_{\text{ox}}\epsilon_0 A}\right)^{-1} = 1.31 \cdot 10^{-15} F, \quad (5.9)$$

where the relative dielectric strength $\kappa_{\text{air}} = 1$, $\kappa_{\text{ox}} = 3.8$, vacuum permittivity $\epsilon_0 = 8.85 \cdot 10^{-12}$ Fm^{-1}, overlap area $A = \pi\left(20 \cdot 10^{-6}\right)^2 = 1.26 \cdot 10^{-9}$ m^2, and gap distance $d_{\text{air}} = 8$ μm and $d_{\text{ox}} = 2$ μm.

Drum deflection measurements are done using the white light interferometer. The voltage is applied using a Delta Electronika ES 0300-0.45 voltage source with manual voltage control. This voltage source can provide a DC voltage up to 300V with 0.5V accuracy and currents of 450 mA. Measurements are done at intervals of 5V for below 20V, 2V between 20V and 34V and 1V above 34V. The intervals decrease with increasing voltage because the electrostatic pressure increases with voltage squared.

5.2 Analysis and results

5.2.1 Drift correction

Because of drift during the measurements, drift correction must be applied to the measurement data. The cross-correlation integral can be used to determine the drift between two images $M_1(x, y)$ and $M_2(x, y)$, which is given as

$$C(l_x, l_y) = \int\int M_1(x, y) M_2(x + l_x, y + l_y) dx dy \quad (5.10)$$

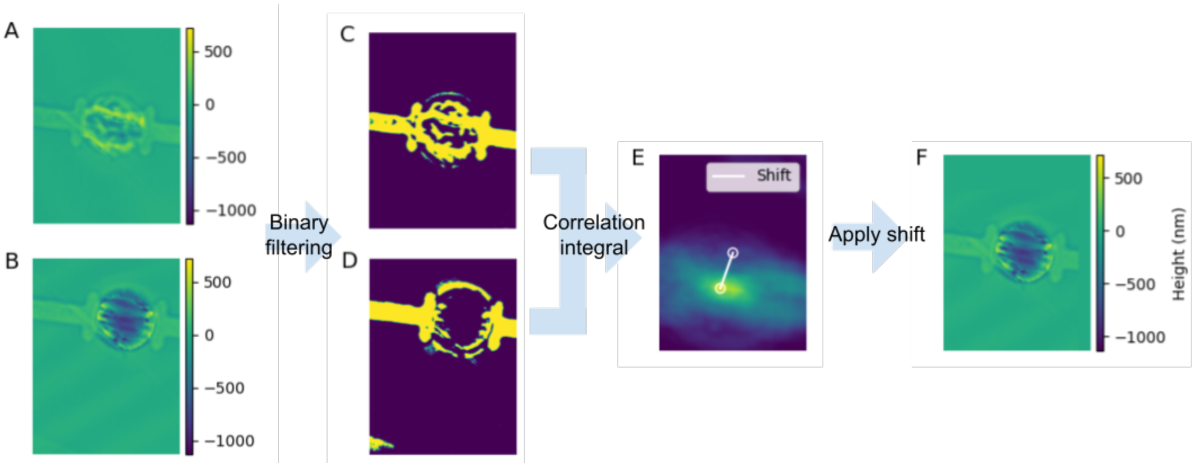

Figure 5.3: Process of determining the shift of **B)** with respect to **A)**. First apply a binary filter to both images to obtain **C,D)**, then compute the correlation integral **E)**. Determine the shift of the maximum value from the center of the image and **F)** apply the shift to the original image to correct for drift.

This integral computes the correlation between two images while shifting the second image across the first. The variables l_x and l_y are the shift of the second image with respect to the first. At the shift values l_x, l_y where the images match best, the correlation integral $C(l_x, l_y)$ has its maximal value. Thus, by finding the maximum of the correlation integral, the drift between measurements can be determined. First applying a binary filter to both images gives a more accurate result, because in the filtered image the two electrodes have a well-defined shape which can be accurately matched. Binary filtering also avoids potential problems that are caused by the difference in deflection of the membrane between measurements, because the membrane height will be below the filter threshold height in all measurement. All measurements are corrected for drift with respect to the first measurement, in order to avoid accumulation of inaccuracies from subsequent corrections. An example of drift correction for measurements with backgate voltages of 0V and -153V is shown in figure 5.3.

Computing a correlation integral is a relatively expensive computation. Since this integral needs to be solved for a range of shift values for each measurement, computing the drift will take a long time. The computation becomes much faster by using Fourier transforms rather than convolution integrals. Since the cross-correlation integral is similar to a convolution integral, it is possible to express it as a product of Fourier transforms. A normal convolution converts to a product of Fourier transforms as follows

$$[f(x,y) * g(x,y)](l_x, l_y) = \int\int f(x,y)g(l_x - x, l_y - y)dxdy \tag{5.11}$$

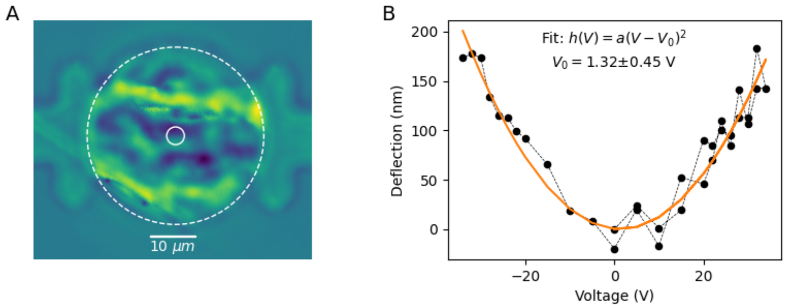

Figure 5.4: **A)** disk with a radius of 10% of the drum radius that is considered the drum center to determine the center deflection, **B)** center deflection over a voltage sweep, with a quadratic function fit.

In the convolution integral, the function $g()$ is flipped because x and y are multiplied by -1. To cast the cross-correlation integral into a convolution integral, the complex conjugate can be used to flip the second function, according to the following rule

$$[f(x,y) * g(x,y)](l_x,l_y) = [f(x,y) * \overline{g(-x,-y)}](l_x,l_y) \tag{5.12}$$

Now the cross-correlation integral can be expressed as a product of Fourier transforms,

$$C(l_x,l_y) = \mathcal{F}^{-1}\left(\mathcal{F}(M_1(x,y)\mathcal{F}(\overline{M_2(x,y)})\right), \tag{5.13}$$

where $\mathcal{F}$ and $\mathcal{F}^{-1}$ denote the Fourier transform and inverse transform respectively. This expression can be solved using a Fast Fourier Transform (FFT) algorithm quickly.

5.2.2 Center point deflection

In order to quantify the deflection of the membrane, the center point deflection is determined by taking the average over a disk with a radius of 10% of the drum radius, see figure 5.4A. Figure 5.4B shows the deflection of the drum over a voltage sweep from 0V to 34V to -34V. In this small deflection regime, the deflection data follows a quadratic shape. A quadratic function with the slope and horizontal offset as fit parameters can be accurately fitted to the data. The offset voltage for this fit is 1.32±0.45 V. This small offset voltage is within the error margin, so the data is symmetric around 0V. This is as expected, since at 0V there is no electrostatic pressure on the membrane. The sweep over the voltage region 0V, 34V, 0V does not show hysteresis, which means that in this regime the flake is deforming elastically and is not slipping over the sample surface.

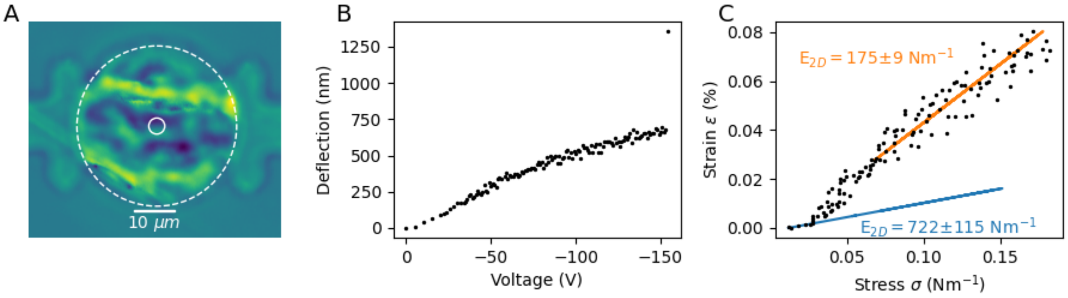

Figure 5.5: **A)** disk with a radius of 10% of the drum radius that is considered the drum center to determine the center deflection, **B)** center deflection over a voltage sweep, **C)** stress-strain curve based on the drum center deflection.

In order to study the effect of strain on the wrinkles in the membrane, in the next experiment the voltage was gradually increased until the drum broke down. Figure 5.5B shows the deflection of the center over a voltage sweep from 0V to -154V. The deflection was again determined from a small disk with radius of 10% of the drum radius, shown in figure 5.5A. At -154V, the deflection increases from 750 nm to 1250 nm, which implies the drum was broken during the voltage increase from -153V to -154V. At roughly -50V there is an inflection point in the voltage-deflection graph, which could correspond to a transition between two different regimes. Figure 5.5C suggests that the membrane is stiffer at low strain values and softens at higher strain values, contradicting the analytical model in [1] that show a lower stiffness in the first regime. The few data points at low stress values that indicate a high stiffness are likely strongly affected by conformational changes of the wrinkles at the membrane center. The slope of the second regime in the stress-strain curve determines the Young's modulus according to the equation

$$\frac{d\sigma}{d\epsilon} = \frac{E_{2D}}{1-\nu} \tag{5.14}$$

The second regime is fitted with a linear function, shown in orange in figure 5.5C, to determine the Young's modulus. The value for the 2D Young's modulus extracted from the slope of this fit according to equation 5.14 is 175±9 Nm^{-1}. Determined using the same analysis, the effective stiffness in the first regime is 722±155 Nm^{-1}. Since this stiffness results from deformation of wrinkles and is determined in the regime where the linear term of the bulge-test equation dominates, it is not related to the Young's modulus but only an effective stiffness in this specific case.

The deflection is a thin membrane is governed by two parameters; the pre-strain and the Young's modulus. The pre-strain determines the linear and the Young's modulus the qubic part of the bulge-test equation. Figure 5.6B

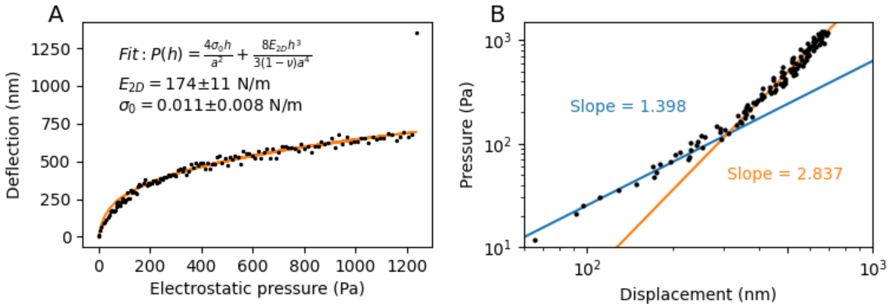

Figure 5.6: **A)** drum center deflection plotted against electrostatic pressure. The data is fitted with the bulge-test equation with fit parameters

shows that the linear term of the bulge-test equation dominates in the low deflection regime and the qubic term dominates in the high deflection regime. This indicates that the high deflection regime can indeed be used to determine the actual Young's modulus, rather than an effective Young's modulus resulting from a mixing of pre-strain and Young's modulus.

The bulge-test equation is a second method to determine the Young's modulus. Figure 5.6A shows the deflection as function of electrostatic pressure. Fitting the bulge-test equation with the pre-strain σ_0 and 2D Young's modulus E_{2D} as fit parameters gives a 2D Young's modulus of $E_{2D} = 174 \pm 11$ Nm^{-1}, which corresponds to the Young's modulus determined from the stress-strain curve. From the same fit, the pre-strain was determined to be $\sigma_0 = 0.011 \pm 0.008$ Nm^{-1}, similar to the value of $\sigma_0 = 0.02$ Nm^{-1} reported in [55] for similar bulge-test measurements.

For higher stress values, the stress-strain curve can also be accurately fitted with the symbolic function proposed in [1]. Figure 5.7A shows a fit of the experimental stress-strain curve with a symbolic function of the analytical model, which is given as

$$\epsilon = \frac{1}{E_{2D}^{f}}\sigma + \frac{1}{2}\left(\frac{\Delta A}{A}\right)_{\max}\left[\frac{\sigma/\sigma_c}{\sigma/\sigma_c + \exp(-(\sigma/\sigma_c) - \beta(\sigma/\sigma_c)^4}\right], \tag{5.15}$$

where $(\Delta A/A)_{\max}$ is the hidden area, σ_c is the critical stress at which the phase transition occurs and E_{2D}^{f} is the Young's modulus. β is a scaling parameter that gives information about the type of wrinkles; if β is close to 0.1 the wrinkles are due to defects and if β is close to 1 the wrinkles are due to prestress. In the fit the stiff regime at low stress values was omitted. The fitting suggests a Young's modulus of 220 ± 11 Nm^{-1} and a critical stress of 0.053 ± 0.1 Nm^{-1}.

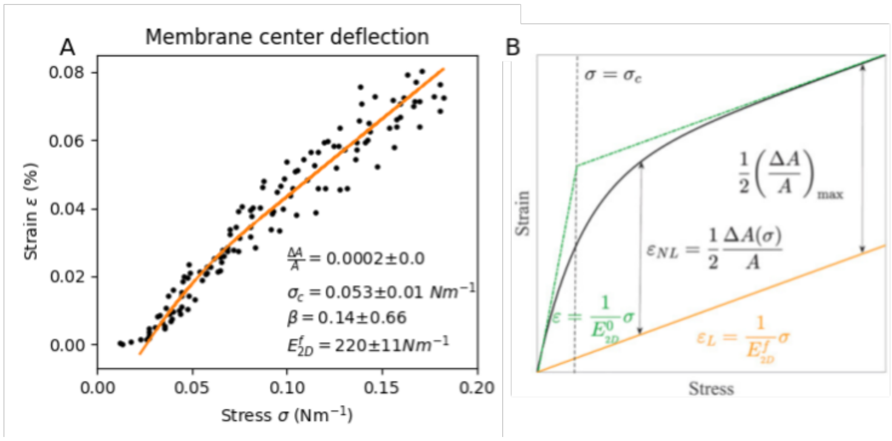

Figure 5.7: Stress-strain curve for the **A)** experimental center deflection with fit of the model and **B)** model for a non-linear stress-strain curve of the membrane center deflection, confirmed by MD simulations [1].

5.2.3 Wrinkle analysis

Because of the large size of the drums and the measurement resolution, it is possible to analyze the membrane wrinkling in more detail. Multiple large elongated wrinkles are visible in the membrane in figure 5.8, with dimensions of 40 μm by 5 μm and up to hundreds of nanometers in height. Figure 5.9 shows a profile of the drum for different voltage values. The red line is the measurement after the drum was broken. Therefore, it is an indicates for the position of the hole under the drum. The profile plots show that the wrinkles shrink in amplitude for increasing potential difference.

Quantifying the degree of wrinkling in a deflected membrane is difficult, because of its deflection curve. This deflection curve can be removed by fitting a theoretical deflection surface to the membrane and subtracting the fit from the data. However, fitting a spherical surface to the deflected membrane is difficult because of the high degree of wrinkling. The fit accuracy can be improved by fitting to an angular average of the membrane profile. The angular average is determined as the mean of a ring with radius r around the drum center, for each value of r. The resulting plots are shown in figure 5.10A, with a fit of a circular function. The fitted function matches the data perfectly at the center and the edge of the drum.

The deviation of the membrane shape from this circular fit can be used as a measure for the degree of wrinkling. The root mean square (RMS) deviation of the membrane from the circular fit is shown in figure 5.10B. In the range between 0V and -75V, the RMS deviation is decreasing, indicating that wrinkles are disappearing. This is also visible in figure 5.10A, where the membrane is

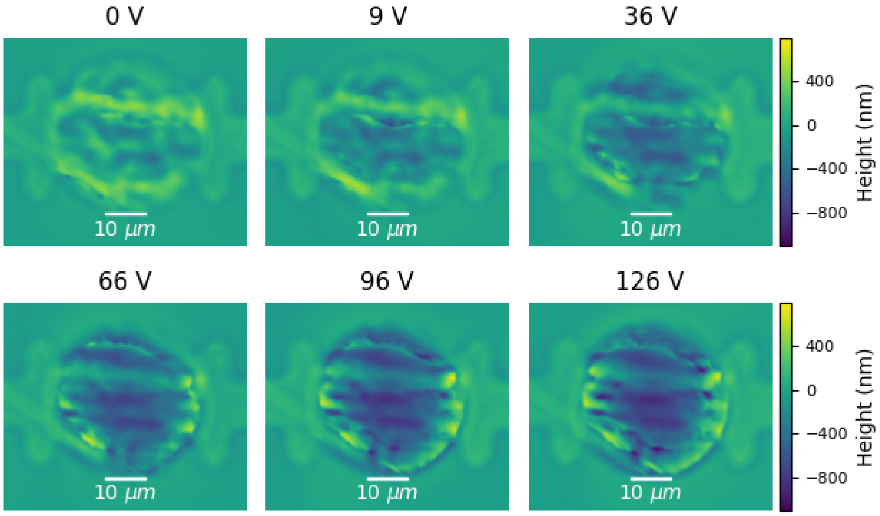

Figure 5.8: Snapshots of the membrane at different backgate voltage values. The color scale indicating the pixel height is the same for all snapshots.

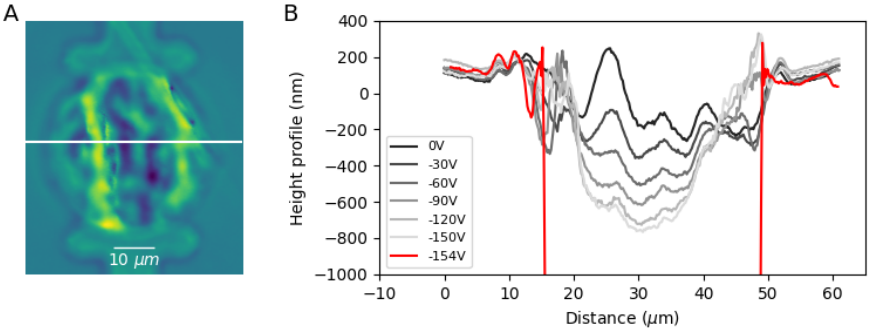

Figure 5.9: **A)** height map of the drum at 0V with a white line with **B)** the profile along this line at different gate voltage values.

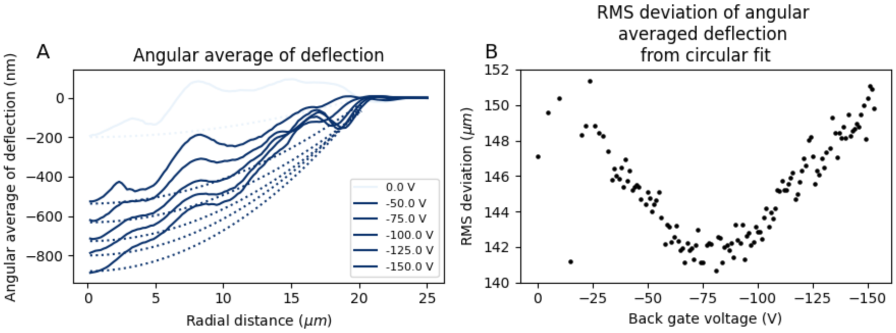

Figure 5.10: **A)** angular average of the membrane with a circular fit, **B)** RMS deviation of the angular average deflection from the circular fit.

getting closer to the circular fit. However, for voltages below -75V the RMS deviation increases again. Figure 5.10A shows that the reason for this increase is a wrinkle roughly at 16 μm that is not flattened with increasing potential difference. It appears that the membrane locally has a higher stiffness, causing this area to not deflect as much as the rest of the membrane. This higher stiffness can be due to a fold or a thickness variation of the graphene. Although this wrinkle at 16 μm remains, the other wrinkles are flattened out with increasing potential difference.

Another way to quantify the degree of wrinkling is to compute the correlation function of the membrane. The correlation function is a measure for the average correlation between points that are a certain distance apart. In a highly wrinkled membrane, the correlation decreases rapidly with increasing distance, whereas in a flat membrane the correlation is high for all distances. The correlation function is given as

$$C(|\bar{r}_1 - \bar{r}_2|) = \langle M(\bar{r}_1)M(\bar{r}_2)\rangle - \langle M(\bar{r}_1)\rangle\langle M(\bar{r}_2)\rangle, \tag{5.16}$$

where $M(\bar{r})$ is the measurement value at pixel position $\bar{r}$ and $\langle ... \rangle$ denotes an average over all pixels. The correlation function of the membrane for different backgate voltage values is shown in figure 5.11A. The correlation length is proportional to the width of the correlation function. Figure 5.11B shows the Full Width at Half Max (FWHM) of the correlation function as a function of backgate voltage. The FWHM is a measure of the width of the correlation function, thus a measure for the correlation length. The FWHM increases with increasing gate potential. This indicates that the membrane flattens when the gate bias increases in absolute value. The advantage of using the correlation function is that is does not depend on the theoretical shape of the deflected membrane, but only takes into account correlations. This makes the effect of a single remaining wrinkle less prominent in the correlation function than in the graph of RMS deviation from a circular fit, as shown in figure 5.10.

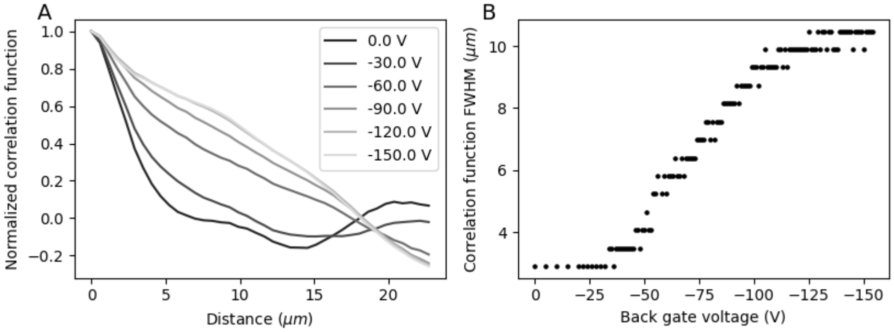

Figure 5.11: Correlation function of the membrane for different values of the gate voltage.

5.3 Conclusion and discussion

Graphene drum deflection measurements are performed by straining the graphene using a electrostatic backgate. The profile of the membrane is measured with white light interferometry with sufficient resolution to distinguish individual wrinkles. In the stress-strain curve based on the deflection of the membrane center, the membrane is first stiffer and then softens. Based on the stress-strain curve, the effective stiffness in the first regime is 722±155 Nm^{-1} and in the second regime the Young's modulus is 175±9 Nm^{-1}. The fact that the stiffness is higher in the more wrinkled regime is surprising. It is likely that the apparent high stiffness in the first regime for the center deflection is due to conformational changes of the wrinkles. An alternative method to compute the Young's modulus is to fit the bulge-test equation. According to this fit, the Young's modulus of the membrane is 174±11 Nm^{-1}. The last method to determine the Young's modulus is by fitting the symbolic function that described the analytical model from [1]. This fit provides a Young's modulus of 220±11 Nm^{-1}. Although the result from fitting the analytical model does not equal the results from the other two methods, the results are reasonable close to conclude that each method is valid.

With a flake thickness of 15±9 nm, the measured 2D Young's modulus of 175±9 Nm^{-1} is equivalent to a 3D Young's modulus of 19.3±11.4 GPa. This 3D Young's modulus is two orders of magnitude smaller than the experimentally determined value of 1 TPa for monolayer graphene using AFM indentation [7], but similar to a value of 58 GPa found in [55] in wrinkled monolayer graphene by bulge-testing. The difference factor of three could be due to the fact that the 3D Young's modulus does not increase linearly with the number of layers of a membrane, leading to a lower 2D Young's modulus for thick membranes and eventually to the 2D Young's modulus of graphite. Other factors that can play a role are non-uniform strain fields, crystal defects and graphene thickness variations. Further research could focus on these factors in order to create drums that reach the theoretical stiffness of graphene. Doing this would require monolayer graphene drums, manufacturing of which is a challenge on its own because of the large drum size.

The average membrane deflection is accurately described by the model proposed in [1]. Because the model is designed for membrane center deflection, the membrane mechanical properties that can be determined by fitting the model to the average membrane deflection are not correct. Nonetheless, the agreement between the model for flattening of a wrinkled graphene and the experimental data shows that indeed wrinkles are flattened by straining the membrane. This is also confirmed by the increasing correlation length of the membrane topology. The conclusion from this study is that wrinkled membranes exhibit non-linear stiffness in the wrinkled phase, but after flattening the wrinkles the stiffness is linear.

Drum deflection measurements with optical interferometric deflection monitoring is a good method to determine the stress-strain curve of a membrane, although local wrinkling at the membrane center can distort the stress-strain curve. The wrinkles can be visualized directly and are visibly decreasing in amplitude with increasing strain. The wrinkles have a large impact of the shape of the deflected membrane, because of which it is hard to fit the theoretical deflection shape. Therefore it is difficult to decouple wrinkling from deflection. In less wrinkled membranes it will be easier to fit the theoretical deflection shape, enabling the decoupling of wrinkling and deflection. This decoupling will reduce the error in the measured deflection and thus the stress-strain curve, but also allow for more detailed investigation of how the shape of individual wrinkles changes under stress.

Bibliography

[1] Ali Sarafraz, Hadi Arjmandi-Tash, Laura Dijkink, Banafsheh Sajadi, Mohsen Moeini, Peter G Steeneken, and Farbod Alijani. Nonlinear elasticity of wrinkled atomically thin membranes. *Journal of Applied Physics*, 130(18):184302, 2021.

[2] Peter Debye and Paul Scherrer. Interferenzen an regellos orientierten teilchen im röntgenlicht. i. *Nachrichten von der Gesellschaft der Wissenschaften zu Göttingen, Mathematisch-Physikalische Klasse*, 1916:1–15, 1916.

[3] Philip Richard Wallace. The band theory of graphite. *Physical review*, 71(9):622, 1947.

[4] DP DiVincenzo and EJ Mele. Self-consistent effective-mass theory for intralayer screening in graphite intercalation compounds. *Physical Review B*, 29(4):1685, 1984.

[5] Kostya S Novoselov, Andre K Geim, Sergei V Morozov, De-eng Jiang, Yanshui Zhang, Sergey V Dubonos, Irina V Grigorieva, and Alexandr A Firsov. Electric field effect in atomically thin carbon films. *science*, 306(5696):666–669, 2004.

[6] Kirill I Bolotin, K J Sikes, Zhifang Jiang, M Klima, G Fudenberg, James Hone, Phaly Kim, and HL Stormer. Ultrahigh electron mobility in suspended graphene. *Solid state communications*, 146(9-10):351–355, 2008.

[7] Changgu Lee, Xiaoding Wei, Jeffrey W Kysar, and James Hone. Measurement of the elastic properties and intrinsic strength of monolayer graphene. *science*, 321(5887):385–388, 2008.

[8] Alexander A Balandin, Suchismita Ghosh, Wenzhong Bao, Irene Calizo, Desalegne Teweldebrhan, Feng Miao, and Chun Ning Lau. Superior thermal conductivity of single-layer graphene. *Nano letters*, 8(3):902–907, 2008.

[9] Rahul Raveendran Nair, Peter Blake, Alexander N Grigorenko, Konstantin S Novoselov, Tim J Booth, Tobias Stauber, Nuno MR Peres, and Andre K Geim. Fine structure constant defines visual transparency of graphene. *Science*, 320(5881):1308–1308, 2008.

[10] E Stolyarova, D Stolyarov, Kirill Bolotin, S Ryu, L Liu, KT Rim, M Klima, M Hybertsen, I Pogorelsky, I Pavlishin, et al. Observation of graphene bubbles and effective mass transport under graphene films. *Nano letters*, 9(1):332–337, 2009.

[11] Vikas Berry. Impermeability of graphene and its applications. *Carbon*, 62:1–10, 2013.

[12] J Scott Bunch, Arend M Van Der Zande, Scott S Verbridge, Ian W Frank, David M Tanenbaum, Jeevak M Parpia, Harold G Craighead, and Paul L McEuen. Electromechanical resonators from graphene sheets. *Science*, 315(5811):490–493, 2007.

[13] Kostya S Novoselov, D Jiang, F Schedin, TJ Booth, VV Khotkevich, SV Morozov, and Andre K Geim. Two-dimensional atomic crystals. *Proceedings of the National Academy of Sciences*, 102(30):10451–10453, 2005.

[14] Yuan Cao, Valla Fatemi, Shiang Fang, Kenji Watanabe, Takashi Taniguchi, Efthimios Kaxiras, and Pablo Jarillo-Herrero. Unconventional superconductivity in magic-angle graphene superlattices. *Nature*, 556(7699):43–50, 2018.

[15] N David Mermin and Herbert Wagner. Absence of ferromagnetism or antiferromagnetism in one-or two-dimensional isotropic heisenberg models. *Physical Review Letters*, 17(22):1133, 1966.

[16] Annalisa Fasolino, JH Los, and Mikhail I Katsnelson. Intrinsic ripples in graphene. *Nature materials*, 6(11):858–861, 2007.

[17] Jannik C Meyer, Andre K Geim, Mikhail I Katsnelson, Konstantin S Novoselov, Tim J Booth, and Siegmar Roth. The structure of suspended graphene sheets. *Nature*, 446(7131):60–63, 2007.

[18] Shikai Deng and Vikas Berry. Wrinkled, rippled and crumpled graphene: an overview of formation mechanism, electronic properties, and applications. *Materials Today*, 19(4):197–212, 2016.

[19] Wenzhong Bao, Feng Miao, Zhen Chen, Hang Zhang, Wanyoung Jang, Chris Dames, and Chun Ning Lau. Controlled ripple texturing of suspended graphene and ultrathin graphite membranes. *Nature nanotechnology*, 4(9):562–566, 2009.

[20] Jianfeng Zang, Changyong Cao, Yaying Feng, Jie Liu, and Xuanhe Zhao. Stretchable and high-performance supercapacitors with crumpled graphene papers. *Scientific reports*, 4(1):1–7, 2014.

[21] Gao Yang, Lihua Li, Wing Bun Lee, and Man Cheung Ng. Structure of graphene and its disorders: a review. *Science and technology of advanced materials*, 19(1):613–648, 2018.

[22] Wenjun Chen, Xuchun Gui, Leilei Yang, Hai Zhu, and Zikang Tang. Wrinkling of two-dimensional materials: methods, properties and applications. *Nanoscale Horizons*, 4(2):291–320, 2019.

[23] Qingzhi Wu, Yaping Wu, Yufeng Hao, Jianxin Geng, Matthew Charlton, Shanshan Chen, Yujie Ren, Hengxing Ji, Huifeng Li, Danil W Boukhvalov, et al. Selective surface functionalization at regions of high local curvature in graphene. *Chemical communications*, 49(7):677–679, 2012.

[24] PZ Sun, Qian Yang, WJ Kuang, YV Stebunov, WQ Xiong, Jin Yu, Rahul Raveendran Nair, MI Katsnelson, SJ Yuan, IV Grigorieva, et al. Limits on gas impermeability of graphene. *Nature*, 579(7798):229–232, 2020.

[25] Wei Yan, Wen-Yu He, Zhao-Dong Chu, Mengxi Liu, Lan Meng, Rui-Fen Dou, Yanfeng Zhang, Zhongfan Liu, Jia-Cai Nie, and Lin He. Strain and curvature induced evolution of electronic band structures in twisted graphene bilayer. *Nature communications*, 4(1):1–7, 2013.

[26] C Wang, Y Liu, L Li, and H Tan. Anisotropic thermal conductivity of graphene wrinkles. *Nanoscale*, 6(11):5703–5707, 2014.

[27] Vesa-Matti Hiltunen, Pekka Koskinen, Kamila K Mentel, Jyrki Manninen, Pasi Myllyperkiö, Mika Pettersson, and Andreas Johansson. Ultrastiff graphene. *npj 2D Materials and Applications*, 5(1):1–7, 2021.

[28] Ryan JT Nicholl, Nickolay V Lavrik, Ivan Vlassiouk, Bernadeta R Srijanto, and Kirill I Bolotin. Hidden area and mechanical nonlinearities in freestanding graphene. *Physical review letters*, 118(26):266101, 2017.

[29] Bing Deng, Zhenqian Pang, Shulin Chen, Xin Li, Caixia Meng, Jiayu Li, Mengxi Liu, Juanxia Wu, Yue Qi, Wenhui Dang, et al. Wrinkle-free single-crystal graphene wafer grown on strain-engineered substrates. *ACS nano*, 11(12):12337–12345, 2017.

[30] Borislav Vasić, Uroš Ralević, Katarina Cvetanović Zobenica, Milče M Smiljanić, Radoš Gajić, Marko Spasenović, and Sten Vollebregt. Low-friction, wear-resistant, and electrically homogeneous multilayer graphene grown by chemical vapor deposition on molybdenum. *Applied Surface Science*, 509:144792, 2020.

[31] Ke Xu, Peigen Cao, and James R Heath. Scanning tunneling microscopy characterization of the electrical properties of wrinkles in exfoliated graphene monolayers. *Nano letters*, 9(12):4446–4451, 2009.

[32] Liusi Yang, Tianxiao Niu, Hui Zhang, Wenjing Xu, Mingchu Zou, Lu Xu, Guoxin Cao, and Anyuan Cao. Self-assembly of suspended graphene wrinkles with high pre-tension and elastic property. *2D Materials*, 4(4):041001, 2017.

[33] Hikari Tomori, Akinobu Kanda, Hidenori Goto, Youiti Ootuka, Kazuhito Tsukagoshi, Satoshi Moriyama, Eiichiro Watanabe, and Daiju Tsuya. Introducing nonuniform strain to graphene using dielectric nanopillars. *Applied physics express*, 4(7):075102, 2011.

[34] Francesca F Settembrini, Francesco Colangelo, Alessandro Pitanti, Vaidotas Miseikis, Camilla Coletti, Guido Menichetti, Renato Colle, Giuseppe Grosso, Alessandro Tredicucci, and Stefano Roddaro. Anisotropic straining of graphene using micropatterned sin membranes. *APL Materials*, 4(11):116107, 2016.

[35] Fen Guan, Piranavan Kumaravadivel, Dmitri V Averin, and Xu Du. Tuning strain in flexible graphene nanoelectromechanical resonators. *Applied Physics Letters*, 107(19):193102, 2015.

[36] Héctor Ochoa, Eduardo V Castro, MI Katsnelson, and F Guinea. Scattering by flexural phonons in suspended graphene under back gate induced strain. *Physica E: Low-dimensional Systems and Nanostructures*, 44(6):963–966, 2012.

[37] Matthias Goldsche, Jens Sonntag, Tymofiy Khodkov, Gerard Jan Verbiest, Sven Reichardt, Christoph Neumann, Taoufiq Ouaj, Nils von den Driesch, Dan Buca, and Christoph Stampfer. Tailoring mechanically tunable strain fields in graphene. *Nano letters*, 18(3):1707–1713, 2018.

[38] Peng Zhang, Lulu Ma, Feifei Fan, Zhi Zeng, Cheng Peng, Phillip E Loya, Zheng Liu, Yongji Gong, Jiangnan Zhang, Xingxiang Zhang, et al. Fracture toughness of graphene. *Nature communications*, 5(1):1–7, 2014.

[39] Kangsik Kim, Jong Chan Yoon, Jaemin Kim, Jung Hwa Kim, Suk Woo Lee, Aram Yoon, and Zonghoon Lee. Dedicated preparation for in situ transmission electron microscope tensile testing of exfoliated graphene. *Applied Microscopy*, 49(1):1–8, 2019.

[40] Jason W Christopher, Mounika Vutukuru, David Lloyd, J Scott Bunch, Bennett B Goldberg, David J Bishop, and Anna K Swan. Monolayer mos 2 strained to 1.3% with a microelectromechanical system. *Journal of Microelectromechanical Systems*, 28(2):254–263, 2019.

[41] H Hugo Pérez-Garza, Eric W Kievit, Grégory F Schneider, and Urs Staufer. Controlled, reversible, and nondestructive generation of uniaxial extreme strains ($>$ 10%) in graphene. *Nano letters*, 14(7):4107–4113, 2014.

[42] Héctor Hugo Pérez-Garza, Eric Walter Kievit, Grégory F Schneider, and Urs Staufer. Highly strained graphene samples of varying thickness and comparison of their behaviour. *Nanotechnology*, 25(46):465708, 2014.

[43] Yong Xie, Jaesung Lee, Hao Jia, and Philip X-L Feng. Frequency tuning of two-dimensional nanoelectromechanical resonators via comb-drive mems

actuators. In *2019 20th International Conference on Solid-State Sensors, Actuators and Microsystems & Eurosensors XXXIII (TRANSDUCERS & EUROSENSORS XXXIII)*, pages 254–257. IEEE, 2019.

[44] Yong Xie, Jaesung Lee, Yanan Wang, and Philip X-L Feng. Straining and tuning atomic layer nanoelectromechanical resonators via comb-drive mems actuators. *Advanced Materials Technologies*, 6(2):2000794, 2021.

[45] Paul Anderson, Yifan Huang, Yuanjun Fan, Sara Qubbaj, Sinisa Coh, Qin Zhou, and Claudia Ojeda-Aristizabal. Signature of multilayer graphene strain-controlled domain walls in quantum hall effect. *arXiv preprint arXiv:2012.13153*, 2020.

[46] M Goldsche, GJ Verbiest, T Khodkov, J Sonntag, N von den Driesch, D Buca, and C Stampfer. Fabrication of comb-drive actuators for straining nanostructured suspended graphene. *Nanotechnology*, 29(37):375301, 2018.

[47] GJ Verbiest, Duo Xu, Matthias Goldsche, Timofiy Khodkov, Shabir Barzanjeh, Nils Von Den Driesch, Dan Buca, and Christoph Stampfer. Tunable mechanical coupling between driven microelectromechanical resonators. *Applied physics letters*, 109(14):143507, 2016.

[48] Andrea Locatelli, Kevin R Knox, Dean Cvetko, Tevfik Onur Mentes, Miguel Angel Nino, Shancai Wang, Mehmet B Yilmaz, Philip Kim, Richard M Osgood Jr, and Alberto Morgante. Corrugation in exfoliated graphene: an electron microscopy and diffraction study. *ACS nano*, 4(8):4879–4889, 2010.

[49] Sophia Dempwolf and Roy Knechtel. Mems 3-axis inertial sensor process. In *2013 Symposium on Design, Test, Integration and Packaging of MEMS/MOEMS (DTIP)*, pages 1–6. IEEE, 2013.

[50] Yi Chen, Xiao-Lei Gong, and Jing-Gang Gai. Progress and challenges in transfer of large-area graphene films. *Advanced science*, 3(8):1500343, 2016.

[51] Andres Castellanos-Gomez, Michele Buscema, Rianda Molenaar, Vibhor Singh, Laurens Janssen, Herre SJ Van Der Zant, and Gary A Steele. Deterministic transfer of two-dimensional materials by all-dry viscoelastic stamping. *2D Materials*, 1(1):011002, 2014.

[52] Kei Kinoshita, Rai Moriya, Momoko Onodera, Yusai Wakafuji, Satoru Masubuchi, Kenji Watanabe, Takashi Taniguchi, and Tomoki Machida. Dry release transfer of graphene and few-layer h-bn by utilizing thermoplasticity of polypropylene carbonate. *npj 2D Materials and Applications*, 3(1):1–8, 2019.

[53] Simone Bertolazzi, Jacopo Brivio, and Andras Kis. Stretching and breaking of ultrathin mos2. *ACS nano*, 5(12):9703–9709, 2011.

[54] Guoxin Cao and Huajian Gao. Mechanical properties characterization of two-dimensional materials via nanoindentation experiments. *Progress in Materials Science*, 103:558–595, 2019.

[55] Ryan JT Nicholl, Hiram J Conley, Nickolay V Lavrik, Ivan Vlassiouk, Yevgeniy S Puzyrev, Vijayashree Parsi Sreenivas, Sokrates T Pantelides, and Kirill I Bolotin. The effect of intrinsic crumpling on the mechanics of free-standing graphene. *Nature communications*, 6(1):1–7, 2015.

[56] Benoit Merle. *Mechanical properties of thin films studied by bulge testing.* Friedrich-Alexander-Universitaet Erlangen-Nuernberg (Germany), 2013.

[57] Xuesong Li, Weiwei Cai, Jinho An, Seyoung Kim, Junghyo Nah, Dongxing Yang, Richard Piner, Aruna Velamakanni, Inhwa Jung, Emanuel Tutuc, et al. Large-area synthesis of high-quality and uniform graphene films on copper foils. *science*, 324(5932):1312–1314, 2009.

[58] AN Obraztsov, EA Obraztsova, AV Tyurnina, and AA Zolotukhin. Chemical vapor deposition of thin graphite films of nanometer thickness. *Carbon*, 45(10):2017–2021, 2007.